On the combined effects of surface tension force calculation and interface advection on spurious currents within Volume of Fluid and Level Set frameworks

Thomas Abadie, Joelle Aubin, Dominique Legendre

On the combined effects of surface tension force calculation and interface advection on spurious currents within Volume of Fluid and Level Set frameworks

T. Abadie [a,b], J. Aubin [b], D. Legendre [a,*]

[a] University of Toulouse, Institut de Mécanique des Fluides de Toulouse CNRS/INPT/UPS, 1 Allée du Professeur Camille Soula, 31400 Toulouse, France
[b] University of Toulouse, Laboratoire de Génie Chimique CNRS/INPT/UPS, 4 Allée Emile Monso, BP-84234, 31030 Toulouse, France

Keywords:
Volume of fluid
Level set
Spurious currents
Continuum surface force
Height function
Taylor flow

A B S T R A C T

This paper deals with the comparison of Eulerian methods to take into account the capillary contribution in the vicinity of a fluid–fluid interface. Eulerian methods are well-known to produce additional vorticity close to the interface that leads to non-physical spurious currents. Numerical equilibrium between pressure gradient and capillary force for the static bubble test case within a VOF framework has been reached in [35] with the height-function technique [14,35]. However, once the bubble is translated in a uniform flow, spurious currents are maintained by slight errors induced by translation schemes. In this work, two main points are investigated: the ability of Volume of Fluid and Level Set methods to accurately calculate the curvature, and the magnitude of spurious currents due to errors in the calculation of the curvature after advection in both translating and rotating flows. The spurious currents source term is expressed from the vorticity equation and used to discuss and compare the methods. Simulations of gas–liquid Taylor flow at low capillary number show that the flow structure and the bubble velocity can be significantly affected by spurious currents.

1. Introduction

Numerical simulations of industrial processes, as well as academic situations often involve two immiscible fluids. A number of computational methods have been developed over the past decade to improve the computation of multiphase flows. The numerical methods to simulate multiphase flows can be classified into two main groups: the "Lagrangian" methods and the "Eulerian" methods. In the first class of methods, the interface is generally tracked using Lagrangian markers, *e.g.* Front-Tracking [49,36] or the Point-Set method [48]. The interface is located explicitly and the calculation of geometrical properties (normal to the interface and curvature) is highly accurate. However, the implementation of such methods in 3D is not straightforward and specific algorithms are needed to deal with the distribution of markers, as well as changes in topology. The second group consists of an implicit representation of the phases in each cell with an additional scalar field. The most common approaches are the Volume of Fluid (VOF) [23,28,7,17] and the Level Set (LS) methods [45,43,22,46]. VOF methods are generally well suited to conserve the mass of the phases and appear to be a natural choice in a finite

http://dx.doi.org/10.1016/j.jcp.2015.04.054

volume framework, while LS methods are known to allow better computation of the geometrical properties of the interface. Eulerian methods have been shown to be well suited to deal with various configurations, including a single bubble rising in a liquid [7], a jet or drop breaking [35,39], coalescence [46], as well as atomization with a number of inclusions of different sizes [19].

Within this Eulerian representation of two-phase flow, great effort has been dedicated to two main features: the transport of the interface and the consideration of capillary forces. When dealing with flows where capillary forces are preponderant, such as the simulation of Taylor flow (or slug flow) in microchannels, care needs to be taken in the computation of surface tension forces. This suggests that the normal to the interface and the curvature need to be accurately estimated. This capillary force located on the interface can be represented in a spatially filtered way using an interface thickness with the Continuum Surface Force method [8] or in a sharp way using the location of the interface at a sub-cell level, *e.g.* Ghost Fluid Method (GFM) [27] and the Sharp Surface Force (SSF) [18]. Within implicit representations of the interface, many methods consider the successive derivatives of the scalar field representing the interface. More recently, [14] and [35] have shown that the construction of height functions allows a better approximation of the interface curvature. Indeed, this method consists of finding the position of the interface with a good accuracy by adding successive volume fractions in a column of fluid (see Section 3.2). Using this height function technique, [35] achieved an exact numerical balance between surface tension forces and pressure jump with the elimination of spurious currents in the case of a static interface. In the case of inviscid fluids where there is no viscous dissipation to balance the kinetic energy produced by spurious currents, [35] still observed a decrease in the intensity of spurious currents over time due to numerical dissipation. The numerical damping of spurious currents when dealing with inviscid fluids was also observed in [12] with a height-function method and a finite-volume compressible flow solver where the intensity of spurious currents decreased to zero after a certain time. This numerical dissipation was further studied in [19] and [12] with the damping of the oscillations of an inviscid droplet. A numerical viscosity was estimated by fitting the damping of the amplitude of the oscillations and as expected, the numerical dissipation decreases as the mesh is refined.

However, it was also shown in [35] that the coupling between transport schemes, surface tension force with Navier–Stokes equations and curvature estimation still needs improvements. [15] showed that the advection step has no direct influence on the spurious currents with a balanced-force surface tension algorithm when the exact curvature is imposed on both cartesian and tetrahedral meshes. However, as it will become clear in Section 4, imposing the exact curvature allows the development of spurious currents to be avoided since the spurious current source term is canceled. In cases of practical interest, the curvature cannot be imposed and the advection step introduces errors in the volume fraction field thereby leading to curvature gradients. As a consequence, the zero velocity field expected in the frame of reference moving with the bubble (like for the static case [35]) is not recovered when the interface is translated in a uniform flow [35,12]. These observations have motivated our work. Different numerical methods implemented in the same flow solver have been compared in terms of the magnitude of spurious currents and pressure jump evaluation on the basis of four test cases: the static bubble case for which a number of results are available in the literature; the translating bubble, which seems more related to physical flows; a bubble in a rotating flow; and the dynamics of Taylor bubble in a circular microchannel. The objective here is to pay attention to the coupling between the interface transport equation and the Navier–Stokes equations. Finally, the dynamics of Taylor bubbles in microchannels is considered because it appears to be representative of the ability of a particular method to deal with spurious currents since these flows are dominated by surface tension (low capillary number and low Weber number). As will be shown, the development of spurious currents in such flows can promote the development of non-physical recirculation areas and consequently, erroneous slip velocity between the bubble velocity and mean velocity in the liquid slug.

2. Numerical schemes

2.1. Spatial and temporal discretizations

The numerical code used for this study is the *JADIM* code, which has been developed to simulate dispersed two-phase flows and used to simulate various multiphase flows systems [7,17,2,29,41,42]. The interface is captured by an Eulerian description of each phase on a fixed grid with variable density and viscosity. Under the assumptions that (*i*) the fluids are Newtonian and incompressible, (*ii*) there is no mass transfer at the interface, (*iii*) the flow is isothermal and (*iv*) the surface tension is constant, the fluid flow can be described by the classical one fluid formulation of the Navier–Stokes equations:

$$\nabla \cdot \mathbf{U} = 0 \,, \tag{1}$$

$$\frac{\partial \mathbf{U}}{\partial t} + (\mathbf{U} \cdot \nabla)\,\mathbf{U} = -\frac{1}{\rho}\nabla P + \frac{1}{\rho}\nabla \cdot \mathbf{\Sigma} + \mathbf{g} + \mathbf{F}_{\sigma,s} \,, \tag{2}$$

where $\mathbf{\Sigma}$ is the viscous stress tensor, $\mathbf{g}$ is the acceleration due to gravity, $\mathbf{F}_{\sigma,\mathbf{s}}$ is the capillary contribution whose calculation is described in Section 3, and ρ and μ are the local density and dynamic viscosity, respectively. The density and viscosity are deduced by linear interpolation from the volume fraction C of one phase in each computational cell:

$$\rho = C\rho_1 + (1 - C)\,\rho_2 \,, \tag{3}$$

$$\mu = C\mu_1 + (1 - C)\,\mu_2 \,, \tag{4}$$

where the volume fraction is $C = 1$ in cells filled with fluid 1, $C = 0$ in cells filled with fluid 2 and $0 < C < 1$ in cells that are cut by the interface. This volume fraction is either calculated directly by solving an advection equation with the VOF method, or deduced from a distance function and the approximation of the Heaviside function as defined by Eq. (5) with the LS method:

$$C = \tilde{H}(\phi) = \begin{cases} 0 & \text{if } \phi < -\varepsilon\,, \\ 0.5\left(1 + \dfrac{\phi}{\varepsilon} + \dfrac{1}{\pi}\sin\left(\dfrac{\pi\phi}{\varepsilon}\right)\right) & \text{if } |\phi| \le \varepsilon\,, \\ 1 & \text{if } \phi > \varepsilon\,, \end{cases} \tag{5}$$

where $\varepsilon = \sqrt{2}\Delta x$ is half the numerical thickness of the interface.

In both cases, VOF and LS, an advection equation is needed to calculate the volume fraction and the distance function respectively. The advection schemes employed in this study are described in the next section.

The equations are discretized on a staggered grid using a finite volume method and all spatial derivatives are approximated using second-order centered schemes. The time scheme used to compute the advective terms in the Navier–Stokes equations is a third-order Runge–Kutta type scheme, while the viscous stresses are solved using a semi-implicit Crank–Nicolson method. The incompressibility is ensured using a projection method, which consists in splitting the velocity field into two contributions: a rotational one, which gives a predicted velocity field calculated semi-implicitly, and a potential one, obtained from a pressure correction solution of a pseudo-Poisson equation, whose divergence is zero. Further details on the numerical algorithms concerning the spatial discretization, as well as the time advancement procedure, can be found in [32,10,30] while details on the interface tracking and related references are given in the following.

2.2. Advection schemes

In this section, we present the advection schemes that have been used to characterize the spurious currents in the different simulations carried out in this work. Whatever the method used in this work, the Eulerian description of the two-phase flow problem involves the advection equation of a scalar ψ:

$$\frac{\partial \psi}{\partial t} + \mathbf{U}\cdot\nabla\psi = 0 \quad \text{with} \begin{cases} \psi = C & \text{(volume fraction) in VOF methods,} \\ \psi = \phi & \text{(signed distance function) in LS methods.} \end{cases} \tag{6}$$

Two different VOF schemes have been used: a geometrical one using a Piecewise Linear Interface Calculation (PLIC) and a second one based on Flux Corrected Transport (FCT) schemes without interface reconstruction. In addition, a Level Set scheme based on the same advection equation but with an additional redistancing equation to keep the level set function as a distance function has been used. These three methods are described below.

2.2.1. VOF-PLIC

In many VOF methods employed to capture a fluid–fluid interface, a reconstruction technique is used to control the thickness of the interface. In the 2-dimensional VOF-PLIC scheme used in this study, the geometrical reconstruction of the interface is based on the *VOF Tools* libraries developed by López and Hernández [31]. The normals used to determine the linear reconstruction are calculated in the same way as those calculated for the surface tension force (see Section 3). From the calculated normals and the given volume fraction at the beginning of the time step, the interface is then represented by a segment in each interfacial cell using the *VOF Tool* libraries [31]. With staggered grids, the volume fraction enclosed in the volume advected by each velocity component can be fluxed through the corresponding cell face. These volumes advected by the velocity components $u_{i,j}$ and $v_{i,j}$ in the x and y directions are respectively $u_{i,j}\Delta t\Delta y$ and $v_{i,j}\Delta t\Delta x$. The interface being approximated by a segment in each interfacial cell, the volume fraction enclosed in these advected volumes is estimated with the *VOF Tool* libraries [31]. The advection scheme is split direction by direction [40]. This implies that despite the volume fraction is fluxed from one cell to another, a small gain or loss of mass can occur. This geometrical reconstruction of the interface with segments (or planes in 3-dimensions) allows a sharp representation of the interface.

2.2.2. VOF-FCT

In the VOF-FCT method implemented in the *JADIM* code, the location and thickness of the interface are both controlled by an accurate algorithm based on Flux-Corrected Transport schemes [51,7]. The advection equation (6) can be written as (with $\psi = C$):

$$\frac{\partial C}{\partial t} + \nabla\cdot(C\mathbf{U}) = C\nabla\cdot\mathbf{U}\,. \tag{7}$$

Despite a divergence free velocity field used for the advection of C ($\nabla\cdot\mathbf{U} = 0$), the scheme is split direction by direction and the velocity field is not divergence free in each direction. Thus, as the volume fraction is not equal in every sub-step, the scheme is not explicitly conservative. In addition, due to the shear normal to the interface, a drawback of the methods without interface reconstruction is the non-physical spreading of the interface over a non-negligible thickness of cells. To correct this excessive spreading of the interface, the velocity field is modified so that the volume fraction of all interfacial

cells in the direction normal to the interface is advected with the velocity on the interface represented by the iso-contour $C = 0.5$. However, the modified velocity field is generally not divergence free and contributes to a gain or loss of mass of one of the phases. To solve this problem, an algorithm that redistributes mass in a global manner is used [7] similarly to what can be done in LS methods by changing the contour representing the interface [11].

While these modifications in the Flux Corrected Transport scheme significantly improve the interface advection [7], the interface still spreads over more than three cells in certain cases, and notably in simulations where the interface is stretched. In addition, for simulations of flows at Reynolds numbers close to one, several hundreds of thousands iterations are often required due to the slow establishment of the flow and the constraint of stability induced by the capillary force [8]. Although the spreading of the interface is not significant during one time step, it can become non-negligible when a large number of iterations are performed. To avoid this unphysical spreading of the interface that leads to the diffuse variation of physical properties, as well as the pressure jump at the interface, a rough cut-off algorithm has been employed when necessary. This consists in imposing the volume fraction $C = 0$ (or $C = 1$) if the volume fraction takes an intermediate value while the interface does not cross the cell, thereby neglecting structures thinner than the dimension of the cell. This results in local gains/losses of mass in proximity of the interface and is therefore applied before the global redistribution of mass.

The algorithm is given in 2-dimensions and the extension to 3-dimensions is straightforward:

$$
\begin{array}{l}
\text{if} \quad \left(0 < C_{i,j} < 1\right) \\
\quad \text{if} \quad \left(C^{-}_{i-nc,j} > 0 \quad \& \quad C^{-}_{i+nc,j} > 0 \quad \& \quad C^{-}_{i,j-nc} > 0 \quad \& \quad C^{-}_{i,j+nc} > 0\right) \\
\qquad \text{if} \quad (C_{i,j} > 0.5) \quad C_{i,j} = 1 \\
\qquad \text{if} \quad (C_{i,j} < 0.5) \quad C_{i,j} = 0
\end{array}
$$

where $C^{-}_{i+k,j+l} = (C_{i,j} - 0.5) \times (C_{i+k,j+l} - 0.5)$ and nc is approximately half the permitted number of cells for numerical thickness. In our cases, $nc = 1$ and 2 have been tested with the test presented in Section 6. It has been found that the cut-off algorithm combined with the velocity extension and global mass redistribution do not significantly change the intensity of the spurious currents (see Appendix A for the comparison). In addition, it has been observed in pure advection tests that there is no spreading of the interface when using fine meshes and as a result the cut-off algorithm is not called during the advection step [1]. Thus, the VOF-FCT advection scheme with interface velocity extension, global mass redistribution and $nc = 2$ seems to be the best compromise between interface thickness and spurious currents and will be used in the following with the notation VOF-FCT. Further details on the effects of each feature of the scheme (velocity extension, mass redistribution and cut-off) on pure advection tests can be found in [7,1].

2.2.3. LS

The Level Set method [45,11] involves a signed distance function instead of a volume fraction in each cell that allows the precise computation of geometrical properties (normal and curvature) of the interface. This precision is ensured by the smooth transition from one phase to the other and is enhanced when the Level Set function gradient magnitude is constant in the domain. The distance function obeys the advection equation (6), which can be written as (with $\psi = \phi$):

$$\frac{\partial \phi}{\partial t} + \nabla \cdot (\phi \mathbf{U}) = 0 \,. \tag{8}$$

The advection of the signed distance function ϕ in Eq. (8) is advanced in time with a third order Runge–Kutta scheme and the advective terms are discretized via a conservative WENO5 scheme [13].

In order to keep the Level Set function as close as possible to a signed distance function, a redistancing procedure is applied using Eq. (9) [43].

$$\frac{\partial \phi}{\partial \tau} + sgn(\phi)\,(|\nabla \phi| - 1) = 0 \,. \tag{9}$$

This partial differential equation is solved using a WENO5 scheme [13,26] for the advective terms and a third order Runge–Kutta scheme for the temporal discretization. The Hamiltonian fluxes are calculated with a Godunov operator.

3. Surface tension force

In capillary flows, care needs to be taken in the calculation of the capillary force $\mathbf{F}_{\sigma,\mathbf{s}} = -\sigma/\rho\,(\nabla \cdot \mathbf{n})\,\mathbf{n}\delta_I$, where σ is the surface tension, $\mathbf{n}$ the normal to the interface and δ_I is the Dirac distribution localizing the interface. The numerical method used to solve the interfacial force is the Continuum Surface Force (CSF) proposed by Brackbill et al. [8]. The surface force $\mathbf{F}_{\sigma,\mathbf{s}}$ is transformed into a volume force $\mathbf{F}_{\sigma,\mathbf{v}}$ by distributing its effects over grid points in the vicinity of the interface in a region that is a few cells thick:

$$\mathbf{F}_{\sigma,\mathbf{v}} = -\frac{\sigma}{\rho}\kappa \nabla C \,. \tag{10}$$

The localization of the interface is available through a non-zero gradient of the volume fraction and the calculation of the curvature κ is detailed in the following.

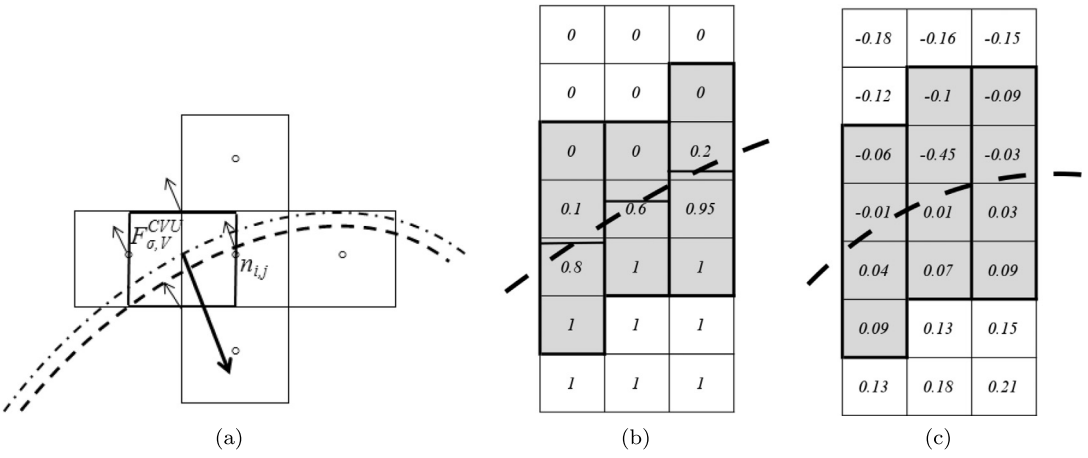

Fig. 1. (a) Schematic representation of the capillary force with a Continuum Surface Force model on staggered grids. Adaptive stencil for the construction of height functions in (b) a Volume of Fluid formulation; (c) a Level Set formulation. The dashed line represents the interface while the dash-dotted line represents the iso-contour where the curvature is calculated in the classic continuum surface force model.

The approaches considered in this work are mostly variants of the CSF method proposed in [8] that differ in the way the curvature is discretized. The manner in which the capillary surface force is converted into a volume force and is spread over the finite volume mesh is not affected except in the Sharp Surface Force (SSF) method [18]. The CSF methods based on the calculation of the curvature by means of the divergence of normal vectors or height functions are differentiated by calling them Classic Continuum Surface Force (CCSF) and Height Function Continuum Surface Force (HFCSF). However, the Sharp Surface Force [18], which roughly sets the pressure jump between cells that are cut by the interface, slightly differs from the Continuum Surface Force in that there is no discretization of a Delta Function to estimate the surface of the interface that cut the interface. The SSF formulation, results in a sharp pressure jump like that obtained with the Ghost Fluid Method [27] or the pressure correction proposed in [36].

3.1. VOF Classic Continuum Surface Force (VOF-CCSF)

From an Eulerian representation involving a scalar function, the geometrical properties of the interface can be calculated from the successive derivatives of the scalar function:

$$\mathbf{n}\delta_I = -\nabla C \,, \tag{11}$$

$$\kappa = -\nabla \cdot \left(\frac{\nabla C}{||\nabla C||} \right) . \tag{12}$$

Since the volume fraction varies from zero to one over a thickness of two to three cells, it has been shown that a smoothing procedure allows a decrease in the errors due to the discretization of the gradient and divergence operators [14,17]. However, [15] also showed that oversmoothing the volume fraction field leads to erroneous results and does not allow a bubble rising in liquid at rest to be simulated correctly. The filtering procedure used in this study has been shown to be able to deal with different two-phase flow problems [7,17,2] and it consists in successively applying a 3×3 convolution matrix ($K_{conv} = [0 \;\; 1/16 \;\; 0 \;;\; 1/16 \;\; 3/4 \;\; 1/16 \;;\; 0 \;\; 1/16 \;\; 0]$) in 2-dimensions to the volume fraction field. In the present simulations, the smoothing step involves 12 and 6 iterations to calculate the curvature and the normal (localization and orientation of the force), respectively, as recommended in [17] in which the same flow solver and the same convolution matrix were used. In *JADIM*, the curvature is calculated at the center of the staggered control volume as illustrated in Fig. 1(a) and the divergence of the unit normal to the interface is calculated in a conservative way [6]:

$$\mathbf{F}_{\sigma,v} = \frac{-\sigma}{\overline{\rho} V} \int_V \nabla \cdot \left(\frac{\nabla C}{\|\nabla C\|} \right) \nabla C dV \tag{13}$$

$$\approx \frac{-\sigma}{\overline{\rho} V} \overline{\nabla C} \int_{\partial S} \left(\frac{\nabla C}{\|\nabla C\|} \right) \cdot \mathbf{n}_{\mathbf{cell}} dS \,, \tag{14}$$

where $\overline{\rho} = (\rho_1 + \rho_2)/2$ is the mean density. Although the use of the mean density is not consistent with the pressure force in Eq. (2), it has been shown to stabilize simulations and decrease the intensity of spurious currents [8]. The gradient of volume fraction in Eq. (14) is discretized in the same way as the pressure gradient in Eq. (2).

3.2. VOF Height Function Continuum Surface Force (VOF-HFCSF)

The height function technique [14,35] allows the geometrical properties of the interface to be calculated accurately from its position, which is obtained by summing the volume fractions of fluid columns. The stencils are oriented along the main component of the normal to the interface and they are adapted in every column until a cell of volume fraction of zero is reached in the direction of negative gradient of volume fraction and a volume fraction of one in the positive direction (see Fig. 1(b)). Once the position of the interface is evaluated, the curvature is calculated from the plane curve $y = f(x)$ via Eq. (15):

$$\kappa = \frac{y''}{\left(1 + y'^2\right)^{3/2}} \,. \tag{15}$$

In addition, the local density in the cell ρ is used in VOF-HFCSF since the use of $\overline{\rho}$ is not necessary for stability purposes with this method.

3.3. LS Classic Continuum Surface Force (LS-CCSF)

In the LS-CCSF method, the same discretization as that used in the VOF-CCSF method (Eq. (14)) is employed.

$$\mathbf{F}_{\sigma,\mathbf{v}} = \frac{-\sigma}{\rho V}\overline{\nabla C}\int_{\partial S}\left(\frac{\nabla\phi}{\|\nabla\phi\|}\right)\cdot\mathbf{n}_{\mathbf{cell}}dS \,. \tag{16}$$

Note that, like in VOF-HFCSF, the local density in the cell ρ is used in LS-CCSF. In CSF methods coupled to Level Set techniques [45], the delta Dirac function is generally approximated by the derivative of the smooth Heaviside function defined in Eq. (5) ($\tilde{\delta}_I = d\tilde{H}(\phi)/d\phi$) and is applied directly while the gradient of the Level Set function is used for calculating the orientation of the force ($\mathbf{n}\delta_I = \nabla\phi/|\nabla\phi|\tilde{\delta}_I$). Here, the curvature is derived from the divergence of the normal to the interface represented by the distance function ($\kappa = \nabla\cdot(\nabla\phi/|\nabla\phi|)$) as it is usually done. However, the difference resides in the estimation of the localization and the orientation, which are both deduced from the volume fraction calculated from the Level Set function (Eq. (5)), *i.e.* $\mathbf{n}\delta_I = -\nabla C$, since natural equilibrium is reached with this formulation as soon as the curvature is uniform along the interface and both the pressure and volume fraction gradients in Eq. (18) are discretized in the same way. We observed in preliminary tests that this formulation (Eq. (16)) provides better results in terms of spurious currents, as well as better convergence rates.

3.4. LS Height Function Continuum Surface Force (LS-HFCSF)

Similarly to the VOF-HFCSF method, in an LS framework the curvature can be estimated from the position of the interface (Eq. (15)) instead of calculating the divergence of the normal to the interface as in the previous section. The Level Set method for the advection equation is the same as in the LS-CCSF method but the curvature is calculated via the position of the interface, which can be found by linear interpolation or more accurately using quadratic interpolations with the four cells surrounding the interface (see Fig. 1(c)). The procedure to locate the interface is the same as that used in [34]. In order to improve the stability of the quadratic interpolations near discontinuities, a minmod operator was introduced in [34] on the second derivatives of the Level Set function calculated on each side of the interface. The curvature is also calculated with Eq. (15).

3.5. LS Sharp Surface Force (LS-SSF)

In the Sharp Surface Force model [18], the surface tension force is non-zero only in the cells crossed by the interface; this is different to the CSF method, which imposes the Laplace pressure jump continuously along the interface. The curvature is calculated following the same procedure as in the LS-CCSF method. For the horizontal direction, if the control volume centered on the x-component of the velocity is crossed by the interface, *i.e.* $\phi_{i-1}\times\phi_i < 0$, the surface tension force is:

$$F_{\sigma,v} = -(\sigma\kappa_I)/(\rho\Delta x) \,, \tag{17}$$

where κ_I is the curvature interpolated on the interface $\kappa_I = \dfrac{|\phi_i|\kappa_{i-1} + |\phi_{i-1}|\kappa_i}{|\phi_i| + |\phi_{i-1}|}$.

4. Origin of spurious currents, vorticity source

In simple cases, such as a static or a translating bubble or drop, the momentum conservation equation (2) reduces to:

$$0 = -\nabla P + \sigma\kappa\nabla C, \tag{18}$$

such that, when taking the curl of Eq. (18), the curvature should satisfy:

$$\nabla\kappa\times\nabla C = 0 \,. \tag{19}$$

Spurious currents are generated when this condition is not satisfied. In the particular case of a surface with a constant curvature (*e.g.* a spherical bubble or drop), the flow will be curl free if the computed curvature is constant. If the curvature is maintained constant during the simulation [18,15], the source term is zero and no spurious currents develop. As a consequence, the elimination of spurious currents requires the use of balanced-force algorithms [18,22,35] with consistent discretization of pressure and capillary forces to satisfy Eq. (18). Curvature gradients as sources of vorticity are identified when writing the vorticity equation from Eq. (2):

$$\frac{\partial \boldsymbol{\omega}}{\partial t} + (\mathbf{U}\cdot\nabla)\,\boldsymbol{\omega} + (\boldsymbol{\omega}\cdot\nabla)\,\mathbf{U} = \frac{\mu}{\rho}\nabla^2\boldsymbol{\omega} - \frac{\sigma}{\rho}\nabla\kappa\times\nabla C\ . \tag{20}$$

From Eq. (20), it is seen that the surface tension force can contribute as a source term for vorticity production when condition (19) is not satisfied. When looking at the initial stage of the simulations, this source term ($\sigma\nabla\kappa\times\nabla C\sim\sigma/D^3$) induces the amplification of vorticity during the first time steps ($\rho\partial\boldsymbol{\omega}/\partial t\sim\rho U_\sigma/(D\Delta t)$) and the corresponding spurious currents are of intensity U_σ given by:

$$U_{\sigma,trans}\sim\frac{\sigma\,\Delta t}{\rho D^2}\ . \tag{21}$$

The spurious currents therefore initially grow linearly with σ as previously observed in [18,15], as well as with the time step [18]. This linear evolution with the surface tension is also in agreement with the dimensional analysis of the momentum equation performed in [15].

When considering long time simulations, Eq. (20) shows that a steady state can be reached for the spurious currents of magnitude U_σ. If viscous effects are dominant, the spurious currents resulting from the vorticity source term are balanced by the viscous term ($\mu\nabla^2\boldsymbol{\omega}\sim\mu U_\sigma/D^3$):

$$U_{\sigma,visc}\sim\frac{\sigma}{\mu}\ . \tag{22}$$

Thus, the intensity of spurious currents can be written using a characteristic capillary number ($Ca=\mu U_{\sigma,visc}/\sigma\sim c$ where c is a constant). This is consistent with previous works [28,39,22,17,50,2,15] in which the magnitude of spurious currents was related empirically to σ/μ.

When inertia is dominating, the spurious currents resulting from the vorticity source term are controlled by the inertia term ($\rho\,(\mathbf{U}\cdot\nabla)\,\boldsymbol{\omega}\sim\rho U_\sigma^2/D^2$) leading to the characteristic velocity:

$$U_{\sigma,in}=\sqrt{\frac{\sigma}{\rho D}}\ . \tag{23}$$

This is the characteristic velocity used in the inviscid problem [35]. These two characteristic velocities are closely related since

$$U_{\sigma,visc}=\sqrt{La}\,U_{\sigma,in}\ , \tag{24}$$

where $La=\dfrac{\rho D\sigma}{\mu^2}$ is the Laplace number. In the tests reported in this work, the Laplace number has been varied in the range 1.2 to 12 000 and the Reynolds number varies within the range [0.69 ; 600]. In this study, $U_{\sigma,visc}$ has been chosen to make the velocities dimensionless.

5. Static bubble

The first test case that we consider is the 2-dimensional static bubble [35]. A cylindrical interface is initialized in a continuous phase without gravity and both fluids have equal density and viscosity. The Laplace number is $La=12\,000$. Only a quarter of the bubble of radius $R_0=0.4$, placed in the bottom left hand side of a square computational domain of length 1 is simulated. Symmetry boundary conditions are applied on the left and bottom boundaries while no-slip boundary conditions are applied on the top and right boundaries. The exact solution of the velocity field should remain zero in the whole domain and the pressure should obey the Laplace pressure jump at the interface.

The analysis of the intensity of spurious currents and pressure jumps is based on the following error norms:

- U_{max} is the maximum absolute velocity in the whole domain and $Ca_{max}=\mu U_{max}/\sigma$ is its dimensionless form used in the following,
- $|\nabla\kappa\times\nabla C|$ is the norm of the source term in Eq. (20) and is used to characterize the vorticity production and the associated spurious currents,
- ΔP_{total} is the pressure jump between the average pressure in the bubble ($C\geq 0.5$) and the average pressure in the continuous phase ($C\leq 0.5$),
- ΔP_{max} is the pressure jump between the maximum and minimum pressure in the domain.

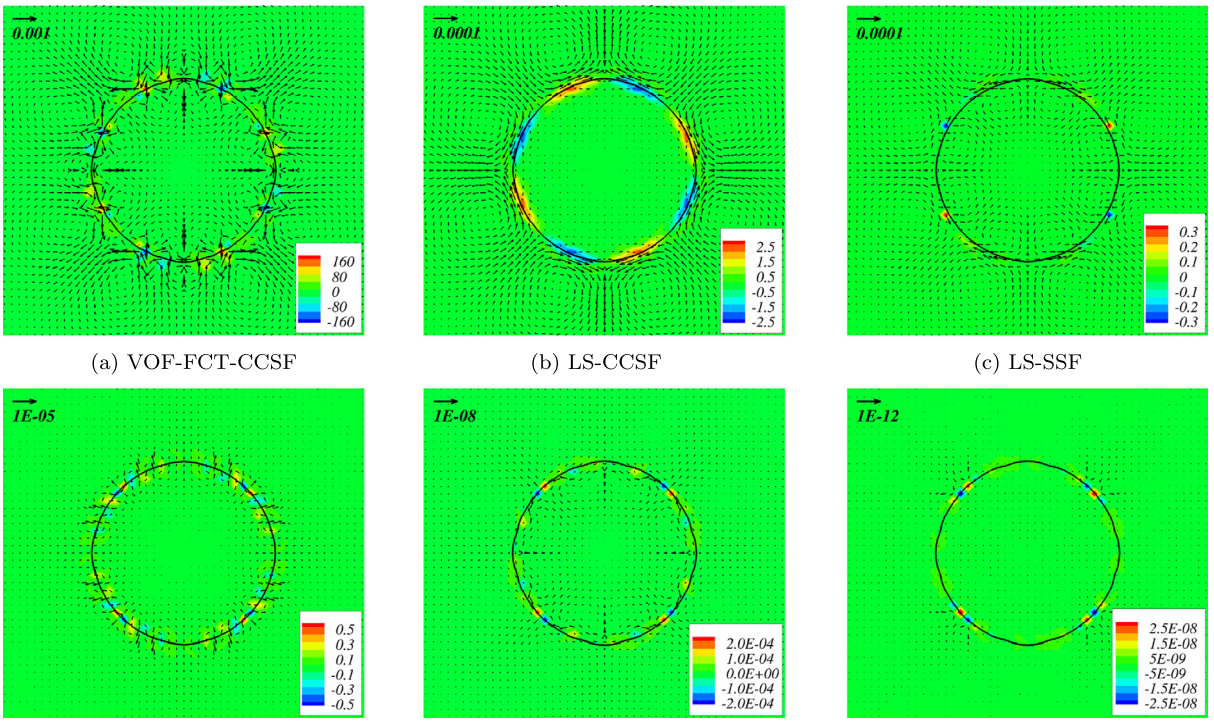

(a) VOF-FCT-CCSF (b) LS-CCSF (c) LS-SSF

(d) LS-HFCSF (e) VOF-FCT-HFCSF (f) VOF-PLIC-HFCSF

Fig. 2. Intensity of the source term $|\nabla\kappa \times \nabla C|$ in the vorticity equation (20) and velocity field (by decreasing spurious currents from (a) to (f)) for $R_0/\Delta x = 12.8$ and $La = 12\,000$.

The numerical parameters considered correspond to those used by Popinet [35] where after a transient evolution, the bubble shape reached a numerical equilibrium with a uniform curvature tangential to the interface, leading to an exact balance between surface tension and pressure forces, and the elimination of spurious currents. Once this numerical balance between pressure and capillary forces is reached, the velocity field is zero, the uniform curvature tangential to the interface keeps the same value over time and the pressure obeys the Laplace pressure jump with an accuracy that is mesh-dependent [35]. The time is made dimensionless with the capillary time scale $t_\sigma^* = \sqrt{\dfrac{\rho D^3}{\sigma}}$.

The relevance of the space discretization between pressure gradient and surface tension force has firstly been tested by imposing the exact curvature in the whole domain for the calculation of $\mathbf{F}_{\sigma,\mathbf{v}}$. The maximum dimensionless velocity in the whole domain reached $Ca_{max} \simeq 5.08 \times 10^{-18}$ showing that Eq. (19) is satisfied to machine accuracy so that the source term in Eq. (20) is negligible and no spurious currents develop. Thus, the exact balance between the volume fraction and pressure gradients is verified and the spurious currents observed in the following can be attributed to the errors in the calculation of the curvature and more precisely, in the gradients of curvature along the interface due to the resolution of a curved interface on a cartesian grid.

Fig. 2 shows the velocity field and the intensity of the source term in the vorticity equation for the different methods. It is clearly seen that the maximum intensities of velocity and vorticity source are collocated.

Fig. 3 shows the evolution of the maximum intensity of the spurious currents with the different methods. Within a VOF framework, it is clearly seen that after approximately $30\,t_\sigma^*$, the height function curvature calculation allows the spurious currents to be decreased by approximately six orders of magnitude with the VOF-FCT-HFCSF method when compared with the standard curvature calculation (VOF-FCT-CCSF) and the spurious velocities are close to machine accuracy with VOF-PLIC-HFCSF, as in [35]. The curvature calculated with the HFCSF methods is exactly located at the interface while it is the mean value of the curvature in the control volume crossed by the interface in CCSF methods (see Fig. 1). The error induced by the location of the curvature calculation promotes curvature gradients, which are source of vorticity in the vicinity of the interface (Eq. (20)). As expected, the Classic Continuum Surface Force method gives better results when coupled with a distance function than a volume fraction. Within an LS framework, Fig. 3 shows that both continuous and sharp methods (LS-CCSF and LS-SSF) are close in terms of the intensity of spurious currents. The similarities in the results obtained with the LS-CCSF and LS-SSF methods are consistent with the observations of [18] who found similar spurious velocities with continuous and sharp surface tension models.

In an LS context, the height function curvature calculation improves the results by more than one order of magnitude. However, the exact balance between pressure and capillary forces that is achieved in a VOF framework, with or without

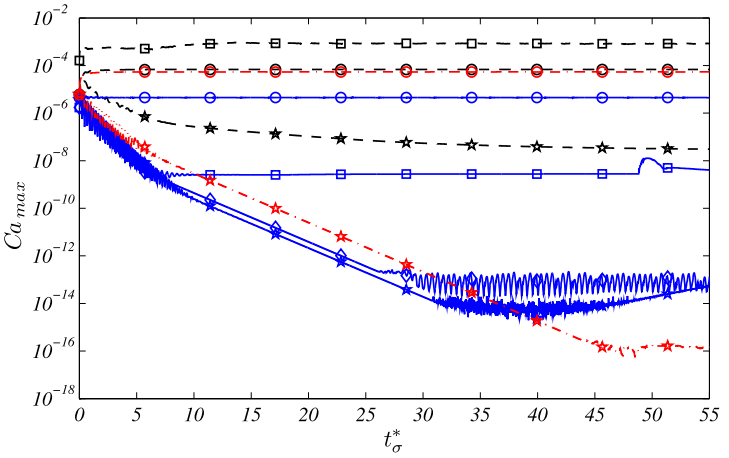

Fig. 3. Evolution of the maximum intensity of the spurious currents in the computational domain over time. Legend: (—□—) VOF-FCT-CCSF; (—⊟—) VOF-FCT-HFCSF; (—◇—) VOF-PLIC-HFCSF; (—◯—) LS-CCSF; (—⊖—) LS-HFCSF; (—⊙·) LS-SSF; (—★—) LS-CCSF without redistancing; (—★—) LS-HFCSF without redistancing; (—★·) LS-SSF without redistancing.

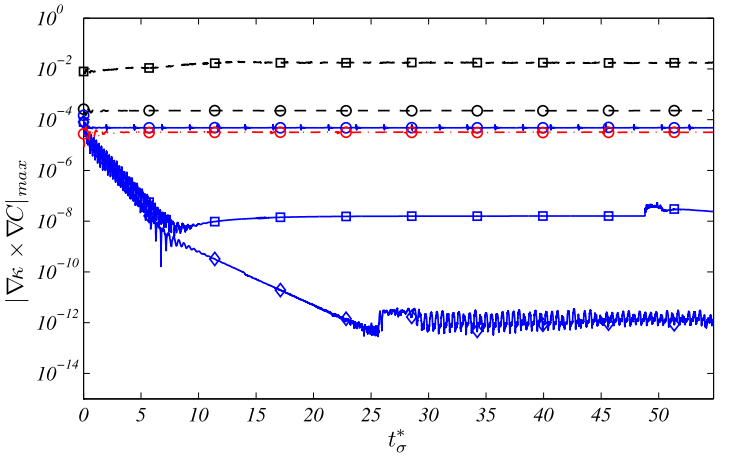

Fig. 4. Evolution of the maximum intensity of the source term $|\nabla\kappa \times \nabla C|$ in the vorticity equation (20) over time. Legend: (—□—) VOF-FCT-CCSF; (—⊟—) VOF-FCT-HFCSF; (—◇—) VOF-PLIC-HFCSF; (—◯—) LS-CCSF; (—⊖—) LS-HFCSF; (—⊙·) LS-SSF.

reconstruction, is not obtained with the LS-HFCSF method. Interestingly, when the redistancing step in the LS transport scheme is skipped, the spurious currents are significantly decreased and it is possible to obtain the exact equilibrium between pressure and capillary forces with both Sharp Surface Force (LS-SSF) and Height Function Continuum Surface Force (LS-HFCSF). Indeed, both methods estimate the curvature at the interpolated position of the interface and the interface oscillates around the position of numerical equilibrium while the velocities tend towards zero. This balance cannot be reached when the redistancing step is activated because the position of the interface (represented by the iso-contour $\phi = 0$) is slightly moved during the redistancing step [34], thereby maintaining the spurious currents. Spurious currents are mainly due to the redistancing step in LS methods when the curvature is calculated on the interface (LS-SSF and LS-HFCSF). Nevertheless, the redistancing step will be used in the following as it is necessary to maintain the level set function as a distance function.

The temporal evolution of the intensity of vorticity source is reported in Fig. 4. A good correlation between this source term and the spurious velocities is observed. Indeed, the curvature gradients and therefore the vorticity source term almost vanish with the VOF-FCT-HFCSF method and are reduced to 10^{-12} with the VOF-PLIC-HFCSF. On the other hand, with the other methods, this vorticity source does not vanish and is balanced by viscous dissipation (see Section 4). These trends are similar to those observed with the maximum intensity of spurious currents.

The balance between pressure jump and surface tension forces observed with both the VOF-FCT-HFCSF and VOF-PLIC-HFCSF methods has been verified for different Laplace numbers ranging from 120 to 12 000 and different meshes involving between 10 and 50 cells per bubble radius. The intensity of spurious currents slightly increases with mesh refinement with the VOF-PLIC-HFCSF method but the maximum spurious currents capillary number remains below 10^{-11}. The spatial convergence of the other methods has been studied and is shown in Fig. 5. As mentioned in [17], the spurious currents

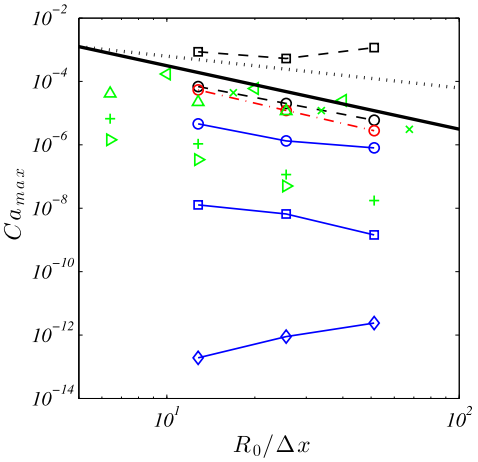

Fig. 5. Convergence with spatial resolution of maximal spurious currents velocities. Legend: (—□—) VOF-FCT-CCSF; (—⊟—) VOF-FCT-HFCSF; (—◇—) VOF-PLIC-HFCSF; (—◯—) LS-CCSF; (—⊖—) LS-HFCSF; (—⊙—·) LS-SSF; (△) Conservative Level Set–Ghost Fluid [16]; (▷) Refined Level Set Grid Method [22]; (◁) VOF-CELESTE [15]; (×) Conservative Level Set-CSF (finite element and $La = 100$) [50]; (+) front-tracking [36]; (· · ·) $U_{max}/U_\sigma \sim (R_0/\Delta x)^{-1}$; (—) $U_{max}/U_\sigma \sim (R_0/\Delta x)^{-2}$.

obtained with the VOF-FCT-CCSF method do not decrease with grid refinement. Since the number of smoothing steps that spreads the interface on a given number of cells has been kept constant, the physical length of smoothing is smaller so that the filter is less efficient when the grid spacing is decreased. [14] drew a similar conclusion about the convergence with mesh refinement of curvature errors computed with a convolution method at the first time step. With a smoothing length proportional to the mesh size ($4\Delta x$ in their study), the rate of convergence of curvature errors is -1 while the rate of convergence is 2 when the smoothing length is not mesh dependent. However, they also mentioned that the ratio of this constant physical length of smoothing over the grid size can become large with fine meshes in order to reach the same accuracy so the convolution would involve a large convolution stencil, leading to non-negligible computational cost. Another possibility would be to use adaptive convolution stencils depending on the ratio of the mesh size over an estimated curvature. Results from the literature are also shown in Fig. 5 and it is seen that the VOF method proposed in [15] in which the curvature is calculated with a least-square fit of second-order Taylor series expansion of the convoluted volume fraction allows the spurious currents to be decreased by several order of magnitudes when compared with standard VOF-CSF method. Interestingly, although the curvature is calculated from a convoluted volume fraction field, the spurious currents show a convergence rate between one and two with mesh refinement. Spurious currents with LS-CCSF, LS-SSF and LS-HFCSF decrease with a rate of convergence close to 2. In addition, both LS-CCSF and LS-SSF agree well with the Conservative Level Set methods of the literature. The present LS-CCSF method and the CLS-CCSF method of [50] show similar spurious current intensities, as well as similar trends. Although the Level Set function in [50] is not a distance function but a smooth regularized indicator function, the curvature, the localization and the normal of the surface tension force are calculated in a similar way as that presented in Section 3.3. A similar Conservative Level Set method is presented in [16], the Level Set function varies smoothly as an hyperbolic tangent across the interface and a Ghost Fluid method is used to calculate surface tension force. It is seen that this method allows the spurious currents to be slightly decreased when compared with LS-CCSF and LS-SSF methods but it also presents a lower rate of convergence. However, it is seen that the height function methods (with LS, VOF-FCT and VOF-PLIC) give better results in terms of parasitic currents. Finally, it is noted that the Refined Level Set Grid method proposed in [22] (where the grid is refined at the interface) leads to very low spurious currents, which are of the same order as those obtained with a front-tracking method in [36] and similar rates of convergence with grid refinement are found.

6. Translating bubble

The second test case consists of a uniform flow field that translates the bubble as proposed in [35]. The previous static case allows to state whether a surface tension scheme is well-balanced or not, and whether the curvature calculation is accurate or not. [15] presented a test case where a bubble is advected and the exact curvature is imposed and showed that no spurious currents develop in agreement with Eq. (19). Here we consider the combined effects of the curvature calculation and the advection of the interface in order to evaluate the precision and the robustness of the coupling between advection schemes, Navier–Stokes solver and capillary term calculation. A uniform horizontal velocity U_0 is imposed in the whole domain with periodic boundary conditions on lateral sides and symmetry boundary conditions on the top and bottom. Both fluids have equal density and viscosity. The cylindrical bubble/droplet should move with the external flow at the same velocity U_0, the velocity field in the frame of reference moving with the bubble should ideally be zero and the pressure field should obey the Laplace pressure jump at the interface.

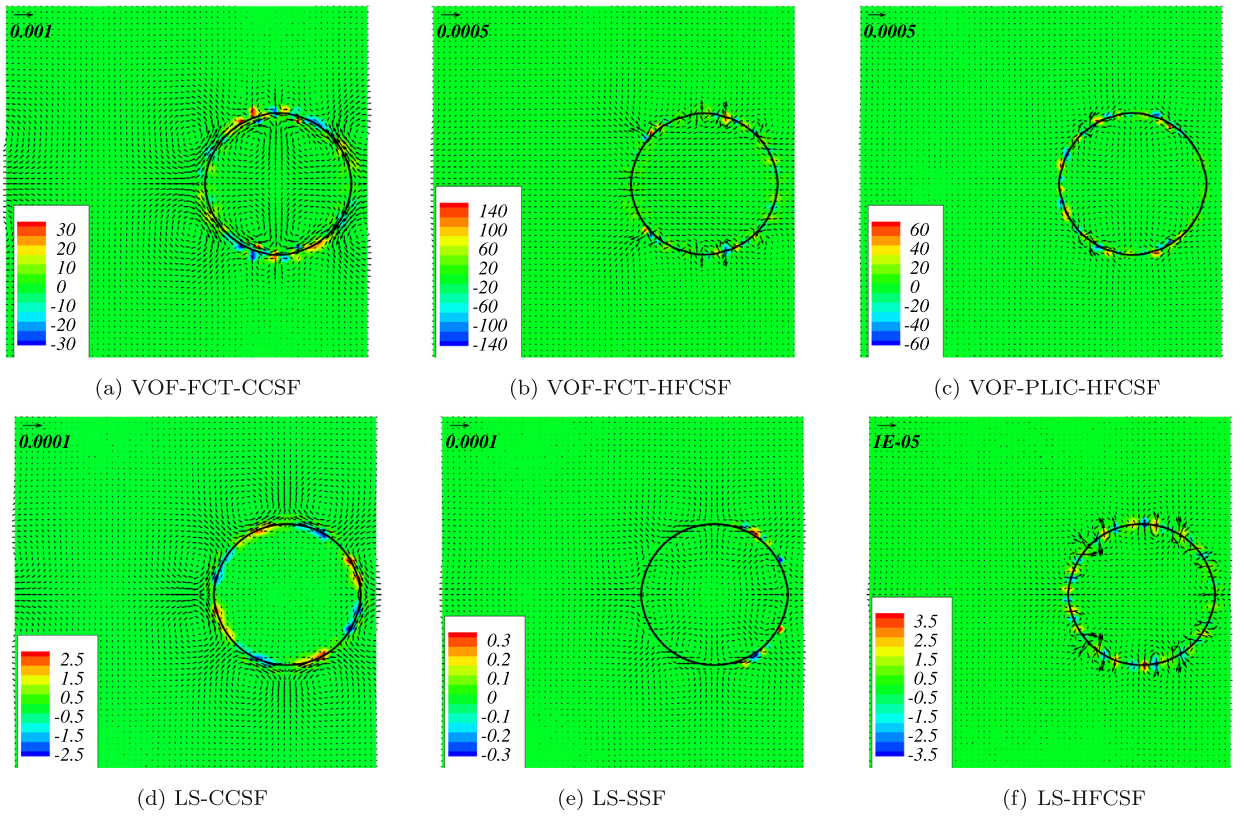

(a) VOF-FCT-CCSF (b) VOF-FCT-HFCSF (c) VOF-PLIC-HFCSF

(d) LS-CCSF (e) LS-SSF (f) LS-HFCSF

Fig. 6. Intensity of the source term $|\nabla\kappa \times \nabla C|$ in the vorticity equation (20) and velocity field after the translation of a distance $1.25D$ in the frame of reference moving with the bubble (by decreasing spurious currents from (a) to (f)) for $R_0/\Delta x = 12.8$, $La = 12\,000$ and $We = 0.4$.

$$(u\ ,\ v)\,(x, y) = (U_0\ ,\ 0)\ , \tag{25}$$

$$p(x, y) = \begin{cases} \dfrac{\sigma}{R_0} & \text{in the bubble,} \\ 0 & \text{outside.} \end{cases} \tag{26}$$

In this test case, the time is made dimensionless with the characteristic advection time $t_0 = D/U_0$. Note that a similar test case with typical gas–liquid density and viscosity ratios is presented in Appendix B. The results obtained in terms of spurious currents are very similar to the tests presented here with density and viscosity ratios of unity.

The spurious velocity and the vorticity production fields obtained with the different methods are shown in Fig. 6. Similarly to the static case, the maximum intensities of vorticity production and spurious velocity are collocated. It is observed that the maximum intensity of spurious currents in VOF-FCT-HFCSF simulation does not tend towards machine accuracy in this test case and is of the same order of magnitude as in the VOF-FCT-CCSF simulation. However, while the spurious velocities are uniformly spread around the interface in the VOF-FCT-CCSF method, the spurious currents are localized in space when using the height function technique for the curvature calculation. This different behavior between the different curvature calculation techniques is also observed with the VOF-PLIC and LS transport schemes. Therefore, the average intensity of spurious currents is decreased with the height function curvature calculation whereas the maximum intensity of spurious currents is of the same order with both the height function and curvature calculation from the divergence of the unit normal to the interface for a given transport scheme.

6.1. Time evolution of spurious currents

The temporal evolution of the maximum velocity of spurious currents is reported in Fig. 7. For a given transport scheme (VOF-FCT, VOF-PLIC or LS), the estimation of the curvature from the height function (HFCSF) leads to similar intensities of spurious currents to those obtained with the calculation of the curvature from the divergence of the unit normal to the interface (CCSF and SSF). The spurious currents obtained with CCSF and SSF methods are in good agreement with those obtained in the static case. On the other hand, with the height function curvature calculation (VOF-FCT-HFCSF, VOF-PLIC-HFCSF, LS-HFCSF), spurious currents are enhanced in this test case when compared with the static case. The accuracy of the height function curvature calculation is therefore highlighted since spurious currents are very sensitive to the errors in the shape that are introduced in the advection step, especially with the VOF-FCT and VOF-PLIC schemes. In this test, it is

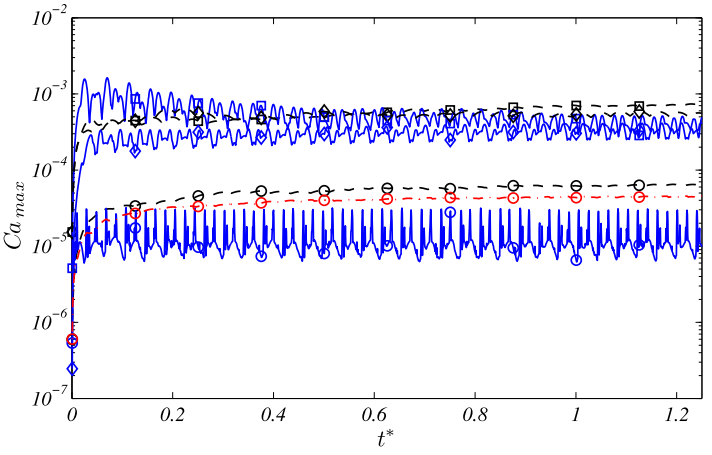

Fig. 7. Temporal evolution of the maximum spurious currents velocity in the frame of reference moving with the bubble for $R_0/\Delta x = 12.8$, $La = 12\,000$, $We = 0.4$. Legend: (–□–) VOF-FCT-CCSF; (–□–) VOF-FCT-HFCSF; (–◇–) VOF-PLIC-CCSF; (–◇–) VOF-PLIC-HFCSF; (–○–) LS-CCSF; (–○–) LS-HFCSF; (–○··) LS-SSF.

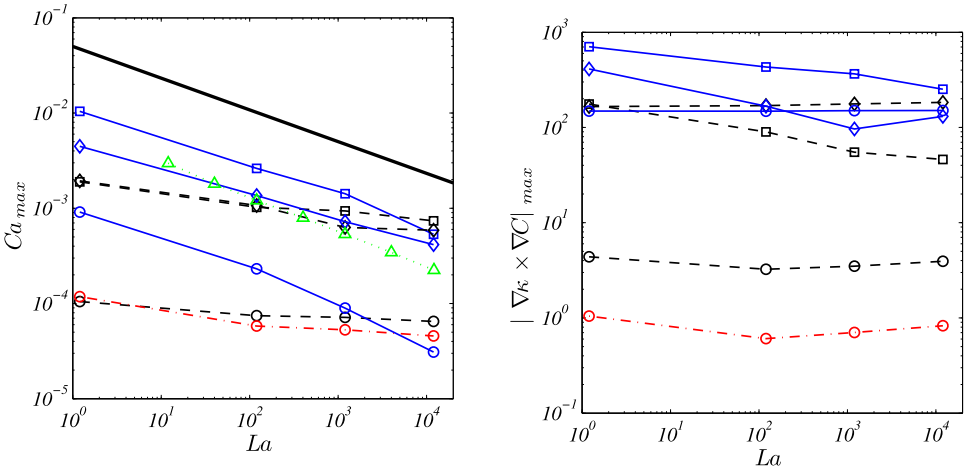

(a) Spurious current intensity

(b) Spurious currents production

Fig. 8. Maximum spurious currents capillary number (a) and vorticity production (b) versus the Laplace number for $R_0/\Delta x = 12.8$ and $We = 0.4$. Legend: (–□–) VOF-FCT-CCSF; (–□–) VOF-FCT-HFCSF; (–◇–) VOF-PLIC-CCSF; (–◇–) VOF-PLIC-HFCSF; (–○–) LS-CCSF; (–○–) LS-HFCSF; (–○··) LS-SSF; (△) VOF-PLIC-HFCSF@*Gerris* [35]; (—) $Ca_{max} \sim La^{-1/3}$.

seen that spurious velocities are induced by the method used to capture and advect the interface. Indeed, this flow configuration shows that VOF-FCT and VOF-PLIC transport schemes generate almost similar spurious currents, with a stronger intensity than that obtained with an LS method, whatever the method used to calculate the curvature and the surface force (continuous or sharp).

6.2. *Effects of the Laplace number*

The effects of fluid properties on the intensity of the spurious currents have first been considered by varying the Weber number. Our results obtained with the VOF-PLIC-HFCSF method are close to those obtained with the *Gerris* collocated finite-volume code in [35] that uses a geometrical VOF transport scheme of the interface (PLIC) and the CSF method is coupled to the height function curvature calculation. With most of the methods, the capillary number based on the maximum intensity of spurious currents does not depend strongly on the Weber number, as mentioned in [35]. Since approximately the same evolution is found with all the methods, we have focused on the effect of the Laplace number on the spurious currents. The evolution of the spurious velocities, in terms of capillary number, as a function of the Laplace number is reported in Fig. 8(a), which also includes results from [35]. Note that in [35], the velocities are made dimensionless with the advective velocity U_0. To compare these results with the present study in terms of characteristic capillary number, the velocities from [35] have been adapted ($Ca_{max}^{[35]} = U_{max}^{[35]}/U_0\sqrt{We_0/La}$). The trend observed in [35] ($U_{max}/U_0 \sim La^{1/6}$) then leads to $Ca_{max} \sim La^{-1/3}$

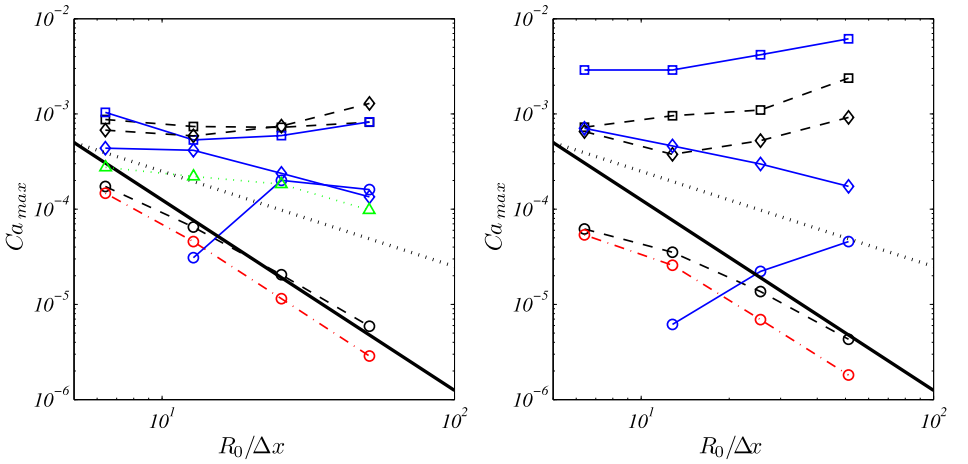

(a) $We = 0.4$ (b) $We = 30$

Fig. 9. Maximum spurious currents capillary number as a function of spatial resolution for $La = 12\,000$. Legend: (–□–) VOF-FCT-CCSF; (–□–) VOF-FCT-HFCSF; (–◇–) VOF-PLIC-CCSF; (–◇–) VOF-PLIC-HFCSF; (–○–) LS-CCSF; (–○–) LS-HFCSF; (–○·) LS-SSF; (△) VOF-PLIC-HFCSF@*Gerris* [35]; (· · ·) $U_{max}/U_{sigma} \sim (R_0/\Delta x)^{-1}$; (—) $U_{max}/U_{sigma} \sim (R_0/\Delta x)^{-2}$.

for a given advective Weber number We_0. Our results obtained with the VOF-PLIC-HFCSF method are in good agreement with the results from [35], despite a slightly lower influence of the fluid properties ($Ca_{max} \sim La^{-\frac{1}{4}}$). Whatever the transport scheme, VOF-PLIC, VOF-FCT or LS, the spurious currents generated with the CCSF method show almost no dependency with the fluid properties and are close to those obtained in the static case. The LS-SSF method also gives similar spurious current intensities and trends to the LS-CCSF method. However, the HFCSF method coupled with either VOF-PLIC, VOF-FCT or LS shows approximately the same trend, with a decrease in the spurious capillary number as the Laplace number increases ($Ca_{max} \sim La^{-\frac{1}{4}}$).

From a general point of view, in the range of Laplace and Weber numbers simulated in the present work ($1.2 < La < 12\,000$ and $0.4 < We < 30$) with 12.8 cells per bubble radius, VOF-FCT-CCSF and VOF-PLIC-CCSF are almost equivalent since the errors in the advection are smoothed. The spurious currents generated with the VOF-PLIC-HFCSF are of the same order of magnitude. The height function coupled with the VOF-FCT transport scheme leads to enhanced spurious currents when compared with the same curvature calculation coupled with the VOF-PLIC transport scheme and this is attributed to the slight interface diffusion. Finally, the spurious currents obtained in an LS framework are reduced by a factor between 2 ($La = 1.2$ and $We = 0.4$) and approximately 100 ($La = 12\,000$ and $We = 30$) when compared with the minimum ones obtained in a VOF framework. It is also interesting to point out that the intensity of the spurious currents in this test case is essentially driven by the transport scheme, *i.e.* LS schemes give better results than VOF-PLIC and finally VOF-FCT transport schemes. However, the trends observed when increasing the Laplace number appear to depend on the method for the curvature calculation, *i.e.* almost no dependency on the Laplace number for the curvature derived from the interface normal and a slight decrease with the height function curvature calculation.

Fig. 8(b) shows the maximum intensity of the vorticity source term and confirms that the vorticity production mainly depends on the transport scheme and the discretization. Indeed, the vorticity production in LS methods is smaller than in VOF methods, except with the LS-HFCSF method where strong curvature gradients, which are localized both in time and space, appear. As expected, the spurious currents production for a given method is constant in a first approximation throughout the range of Laplace numbers considered despite slight variations due to the coupling between spurious velocities, advection errors, curvature gradients and vorticity production. These observations show that the decrease in spurious currents as the Laplace number increases is not related to a decrease in vorticity production. Thus, the development of the vorticity source term into spurious currents and the balance between them depends on the Laplace number.

6.3. Convergence with spatial resolution

6.3.1. Intensity of spurious currents

The convergence with spatial resolution of the maximum velocity is shown in Fig. 9 for a given Laplace number ($La = 12\,000$) and two different Weber numbers ($We = 0.4$ and $We = 30$). As observed in [17] for the static case, VOF-FCT-CCSF does not converge with spatial resolution and this is also true for the VOF-PLIC-CCSF method since both methods behave similarly as explained before. It is not surprising that a slight increase in spurious currents with increasing the number of nodes is observed since the number of smoothing iterations is kept constant and thus, the filtering procedure acts over a thinner region. VOF-FCT-HFCSF does not converge either when the number of nodes is increased and the trend is even worse with the LS-HFCSF method. VOF-PLIC-HFCSF presents almost a first order convergence rate. These different behaviors with a

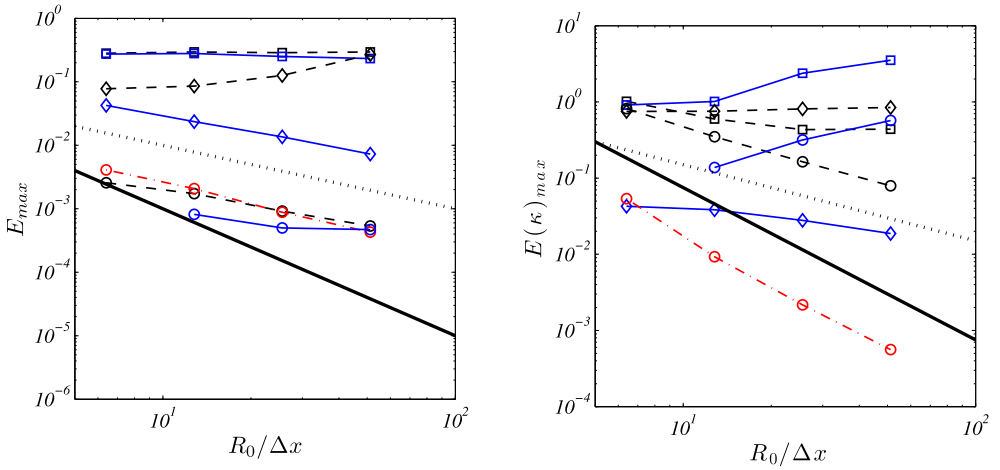

(a) Maximum shape error

(b) Maximum curvature error

Fig. 10. Shape errors (a); curvature errors (b) as a function of spatial resolution for $La = 12\,000$ and $We = 30$. Legend: (–□–) VOF-FCT-CCSF; (–□–) VOF-FCT-HFCSF; (–◇–) VOF-PLIC-CCSF; (–◇–) VOF-PLIC-HFCSF; (–○–) LS-CCSF; (–○–) LS-HFCSF; (–○·) LS-SSF; LS-SSF; (· · ·) $E \sim (R_0/\Delta x)^{-1}$; (–) $E \sim (R_0/\Delta x)^{-2}$.

given curvature calculation and different transport schemes show the importance of the errors introduced in the advection step that are captured with an accurate curvature calculation, such as the height function method. Finally, LS-CCSF and LS-SSF present near second order convergence rates. The methods show similar trends within the range of Weber numbers considered. The differences reside in slightly lower rates of convergence at $We = 30$ and the spurious velocities obtained with the VOF-FCT scheme are greater than those at $We = 0.4$. Since there is no major difference and the calculation time is found to decrease when the bubble velocity increases (*i.e.* for high Weber numbers), all other spatial convergence studies have been carried out at $We = 30$.

6.3.2. Shape errors

It is interesting to note the consistency between the previous observations about spurious currents and the errors on the shape of the bubble, E_{max} and its curvature, $E(\kappa)_{max}$ after translation. Indeed, it is shown in Fig. 10(a) that the error on the shape is minimized with the LS method and is maximum with the VOF-FCT transport scheme. Despite the different shape errors obtained with VOF-FCT-CCSF and VOF-PLIC-CCSF methods, the errors on the calculated curvature are similar due to the smoothing procedure used. However, with the height function curvature calculation, spurious currents arise due to the advection of the interface and it is not surprising to observe an increase in the curvature errors with the VOF-FCT-HFCSF method when compared with the VOF-PLIC-HFCSF method, which minimizes the advection errors in a VOF framework. While the error on the shape decreases with grid refinement with the LS-HFCSF method, the maximum error on the curvature and the vorticity source term increase, as it is the case with the maximum spurious velocity. It is observed with the LS-CCSF that the maximum curvature errors are enhanced when compared with LS-SSF or VOF-PLIC-HFCSF methods whereas the spurious currents generated are lower to those obtained with the VOF-PLIC-HFCSF method and similar to those obtained with the LS-SSF method. This can be due to the fact that the same accuracy is achieved in the curvature calculation for both the sharp and continuous formulations but the difference resides in the interpolation of the curvature at the interface in the sharp formulation. Thus, the LS-CCSF introduces a gradient of curvature normal to the interface, while the main contribution in the generation of spurious currents comes from the tangential gradient (see Eq. (19)). [38] conducted a similar mesh convergence study of curvature errors with the translation of a circle. It is interesting to note that although the Navier–Stokes equations were not solved in their advection test, the curvature errors did not converge either with mesh refinement in a VOF framework with the curvature calculated from the divergence of the unit normal to the interface, which is in agreement with the results presented for the VOF-FCT-CCSF and VOF-PLIC-CCSF schemes in Fig. 10(b). However, they did not observe convergence of the curvature errors with a Level Set function when refining the mesh, while first and second order convergence rates are observed with LS-CCSF and LS-SSF methods respectively. This is probably due to the fact that their Level Set function is used in the framework of a CLSVOF method and it has been observed that the order of convergence of curvature and spurious currents is around one order lower with CLSVOF methods than with LS methods in the case of a static bubble [33]. In addition, [38] presented a new method consisting of advecting the normals to the interface in order to compute normals and curvatures accurately. Close to second order convergence rate was obtained with translation and rotation advection tests.

In addition, the rates of convergence of the maximum curvature error for the different methods are close to those obtained for the maximum spurious current intensity. Indeed, going back over the dimensional analysis presented in Section 4 using the mesh size as the characteristic length rather than the bubble diameter, the rates of convergence with spatial reso-

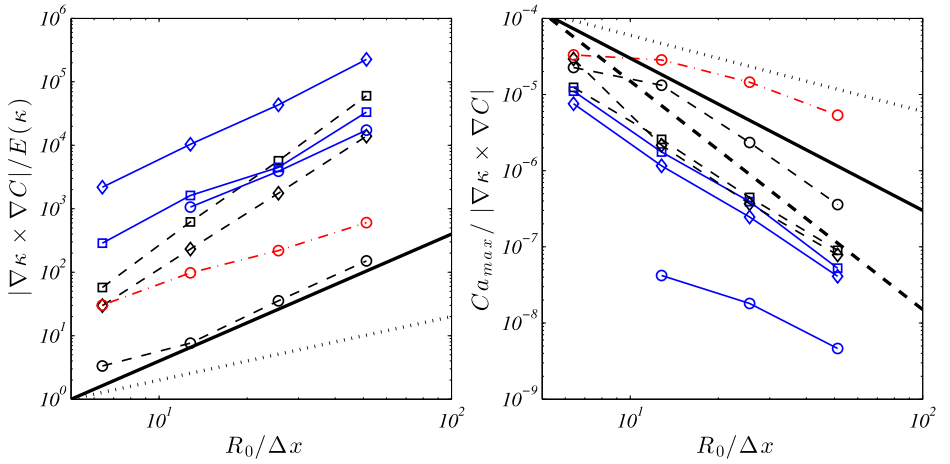

(a) Vorticity source vs curvature error

(b) Velocity vs vorticity source

Fig. 11. Ratio of vorticity source term to curvature error (a) and ratio of spurious currents capillary number to vorticity source term (b) as a function of the spatial resolution $La = 12\,000$ and $We = 30$. Legend: (–□–) VOF-FCT-CCSF; (–⊡–) VOF-FCT-HFCSF; (–◇–) VOF-PLIC-CCSF; (–◈–) VOF-PLIC-HFCSF; (–○–) LS-CCSF; (–⊖–) LS-HFCSF; (–⊖·) LS-SSF. (a) (· · ·) $E \sim (R_0/\Delta x)$; (—) $E \sim (R_0/\Delta x)^2$. (b) (· · ·) $E \sim (R_0/\Delta x)^{-1}$; (—) $E \sim (R_0/\Delta x)^{-2}$; (– – –) $E \sim (R_0/\Delta x)^{-3}$.

lution of the velocity, vorticity production and curvature can be related. The use of this characteristic length is justified since the present analysis concerns spurious flows where the derivatives in the vorticity equation (20) quantify errors over the mesh (discretization errors, as well as spurious velocity and vorticity fields gradients) instead of variations due to physical phenomena, which would be related to physical characteristic lengths (*e.g.* the bubble diameter). Thus, the vorticity source term is written as a function of the error in the curvature calculation as follows:

$$\nabla\kappa \times \nabla C \sim \frac{E(\kappa)}{\Delta x^2} \tag{27}$$

In addition, the balance between vorticity production and the viscous term can then be written as:

$$\mu \frac{\omega_{max}}{\Delta x^2} \sim \sigma \nabla\kappa \times \nabla C \tag{28}$$

$$i.e. \quad \frac{Ca_{max}}{\Delta x^3} \sim \nabla\kappa \times \nabla C \tag{29}$$

Fig. 11(a) shows the ratio of vorticity production to curvature error as a function of the mesh size. Good agreement with Eq. (27) is observed (divergence of order 2) for all the methods. It is interesting to point out that for a given curvature error, the vorticity source term is minimized with standard curvature calculations when compared with height function since the curvature errors are localized in space and the curvature gradient is enhanced while it is spread along the interface with smoothed methods (CCSF). Fig. 11(b) shows the ratio of maximum spurious current intensity to the vorticity source term as a function of the spatial resolution. It is seen that this ratio decreases as the mesh size decreases whereas the rate of convergence is approximately one order lower than the one expected from Eq. (29), *i.e.* close to second order convergence instead of third order. This decrease in the rate of convergence is attributed to non-linear effects in the vorticity equation. As a consequence, curvature errors and maximum spurious current intensity show similar rates of convergence with spatial resolution ($\sim |\nabla\kappa \times \nabla C|\Delta x^2$). Finally, note that for a given vorticity production, the VOF methods minimize the spurious capillary number when compared with LS methods (see Fig. 11(b)) except for the LS-HFCSF method where strong oscillations of the curvature and the vorticity source term occur instantaneously and lead to a decreased ratio of spurious current intensity to vorticity source term. These observations allow us to conclude that spurious currents, vorticity production and curvature gradients are closely related. The sensitivity of the vorticity production to the transport scheme and the advection errors is enhanced with the height function curvature calculation when compared with the smoothed standard curvature calculation.

6.3.3. Laplace pressure jump

Another feature of the coupling between the surface tension scheme, the curvature calculation and the transport scheme is the accuracy in the pressure jump estimation. The decrease in spurious velocities does not necessarily lead to a better pressure jump calculation. Indeed, the pressure jump depends on the error on the curvature while spurious currents are related to its derivative since the source of vorticity resides in curvature gradients tangential to the interface. For instance, [17] showed that increasing the number of iterations in the filtering procedure of the volume fraction leads to a decrease in spurious velocities but the numerical thickness of the pressure jump increases with filtering and a compromise therefore

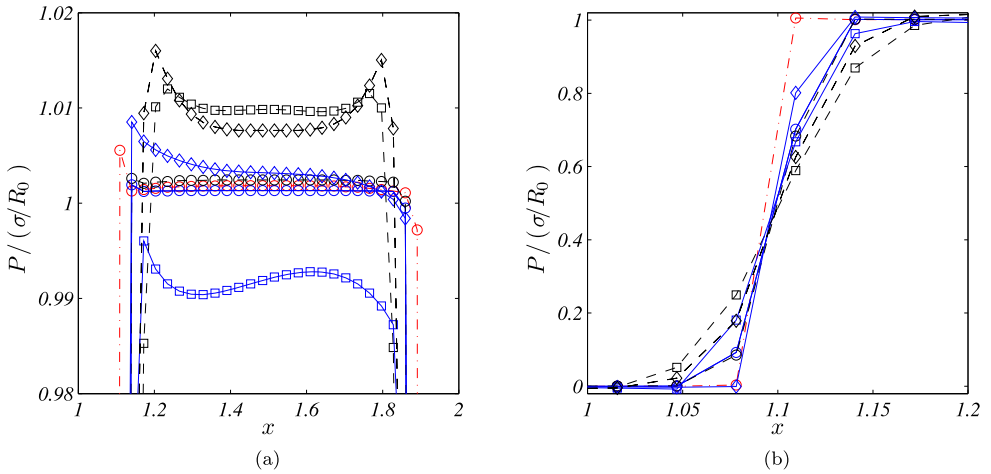

Fig. 12. Normalized pressure jump. Close up of (a) the pressure in the bubble; (b) the pressure jump at the bubble rear cap. Legend: (–□–) VOF-FCT-CCSF; (–□–) VOF-FCT-HFCSF; (–◇–) VOF-PLIC-CCSF; (–◇–) VOF-PLIC-HFCSF; (–○–) LS-CCSF; (–○–) LS-HFCSF; (–○·) LS-SSF.

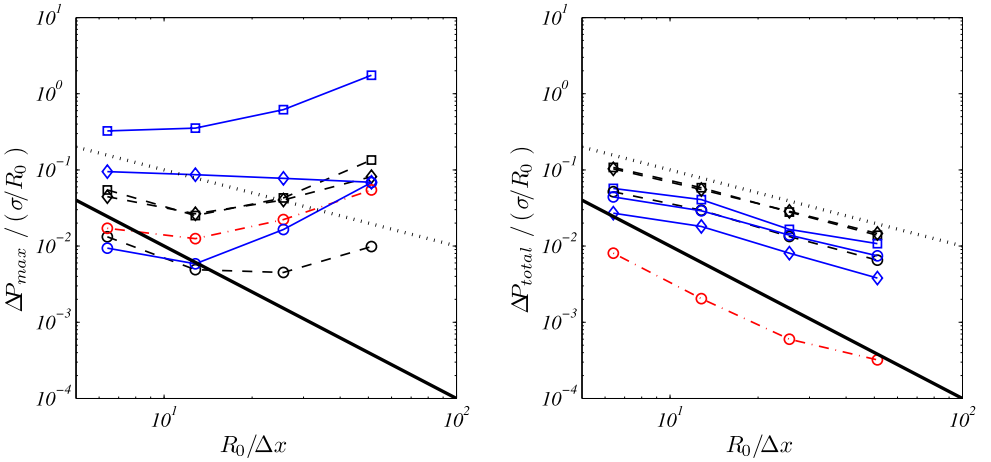

Fig. 13. Pressure errors as a function of spatial resolution for $La = 12\,000$ and $We = 30$. Legend: (–□–) VOF-FCT-CCSF; (–□–) VOF-FCT-HFCSF; (–◇–) VOF-PLIC-CCSF; (–◇–) VOF-PLIC-HFCSF; (–○–) LS-CCSF; (–○–) LS-HFCSF; (–○·) LS-SSF; (· · ·) $E \sim (R_0/\Delta x)^{-1}$; (—) $E \sim (R_0/\Delta x)^{-2}$.

needs to be found to accurately calculate the Laplace pressure jump. In the present simulations, the errors in the pressure jump were generally insensitive to the changes in the Weber number and no explicit tendency was observed with the Laplace number. Fig. 12 shows the pressure profile through the bubble along the horizontal plane of symmetry. It is seen in Fig. 12(a) that the pressure at the center of the bubble is better calculated within an LS framework (less than 0.3% error) than in a VOF framework. Although the pressure at the center of the bubble with the VOF-PLIC-HFCSF method is not so far from the pressure estimated in the LS simulations, the pressure field has peaks around the interface, whereas it is much more uniform in an LS framework.

Fig. 13(a) reports the maximum pressure jump errors as a function of spatial resolution. No convergence with grid spacing is observed with any method. The importance of the transport scheme when using the height function curvature calculation is again highlighted. The VOF-PLIC transport scheme allows the maximum pressure jump errors to be significantly decreased when compared with the VOF-FCT advection scheme. However, the errors remain greater than those obtained with either VOF-FCT-CCSF or VOF-PLIC-CCSF methods, which are again similar. The LS methods and mainly the LS-CCSF method allow the maximum pressure jump errors in the domain to be minimized. Finally, the transition region of the pressure jump across the interface at the bubble rear cap is illustrated in Fig. 12(b) and quantified with the spatial convergence of the error on the total pressure jump $\Delta P_{total}/(\sigma/R_0)$ in Fig. 13(b). It is seen that compared with the continuous formulation of the surface tension force, the height function reduces the transition region and especially within a VOF framework since the smoothing procedure applied to reduce spurious currents in the CCSF methods spreads the pressure jump. However, it is clear that the sharp surface force is the most accurate since there is no numerical thickness of the

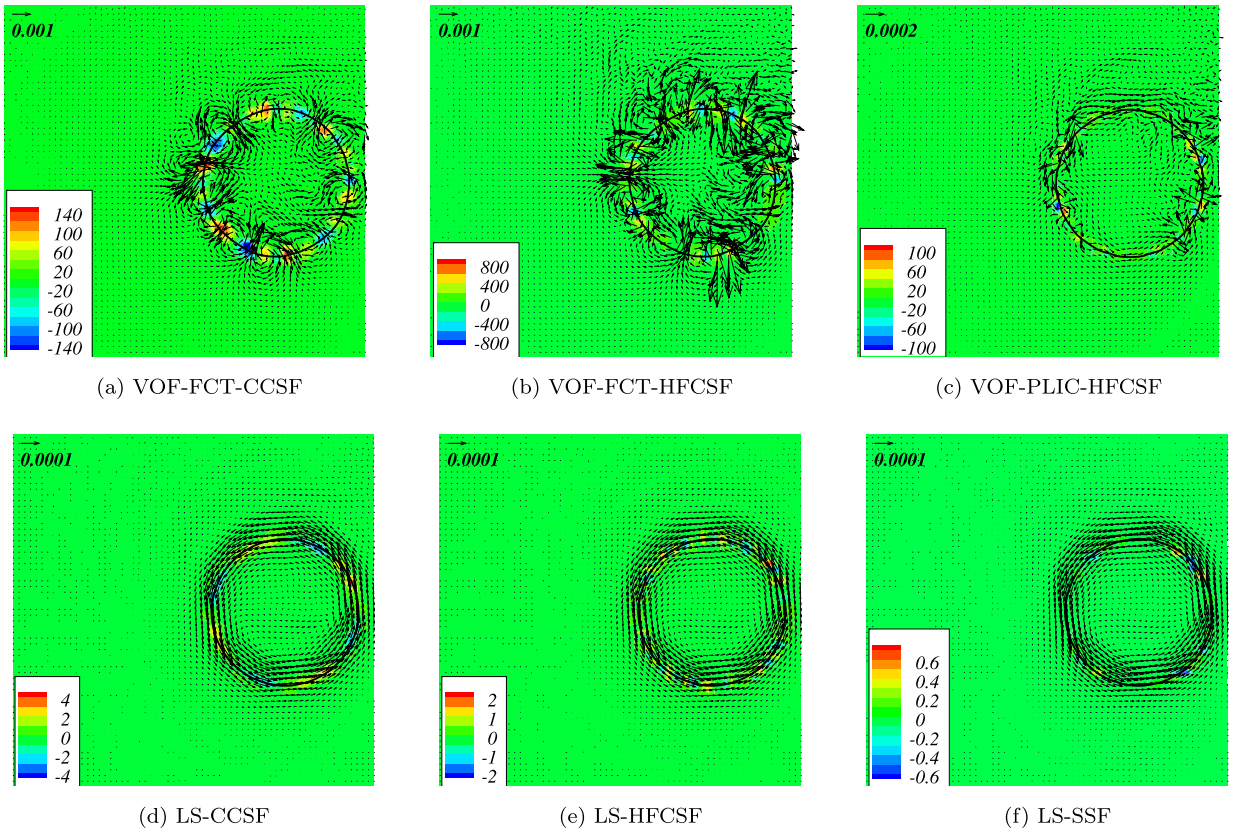

(a) VOF-FCT-CCSF (b) VOF-FCT-HFCSF (c) VOF-PLIC-HFCSF

(d) LS-CCSF (e) LS-HFCSF (f) LS-SSF

Fig. 14. Intensity of the source term $|\nabla\kappa \times \nabla C|$ in the vorticity equation (20) and velocity field after the translation of a distance $1.25D$ in the frame of reference moving with the bubble (by decreasing spurious currents from (a) to (f)) for $R_0/\Delta x = 12.8$, $La = 12\,000$ and $We = 0.4$.

interface. The LS-SSF method also shows a better rate of convergence (slightly less than 2) than all the other methods, which all converge with first order.

7. Rotating bubble

A bubble placed in a rotating flow has been used previously to characterize the efficiency of the transport scheme [6] but not to study the efficiency of the coupling between interface advection and the surface tension force. This test is interesting since the displacement is not uni-directional like for the translating bubble, which moves along the mesh direction. Theoretically, the velocity in the frame of reference moving with the bubble should be zero, providing there are no spurious currents. Although the pressure in each phase is not constant due to the advective terms of the Navier–Stokes equations, which are not null in this case, the pressure jump at the interface still obey the Laplace law since no viscous shear stress is induced by the rotating flow field given by Eq. (30). The theoretical velocity and pressure fields are given by Eqs. (30)–(31). Images of the configuration and the spurious currents generated in such a flow after one revolution are illustrated in Fig. 14.

$$(u\,,\,v)\,(x,y) = (\,U_0 \times y\,,\,-U_0 \times x)\,, \tag{30}$$

$$p(x,y) = \frac{\rho U_0^2}{2}\left((x-x_0)^2 + (y-y_0)^2\right) + \begin{cases} \dfrac{\sigma}{R_0} & \text{in the bubble,} \\ 0 & \text{outside.} \end{cases} \tag{31}$$

The evolution of the maximum intensity of spurious currents with time is reported in Fig. 15. In this test case, which is slightly more complex, the predominant effects of the transport scheme on the spurious currents that have been observed with the translating case are enhanced. Fig. 15 shows that the spurious currents are clearly controlled by the transport scheme. Indeed, with both curvature calculations, the use of the VOF-PLIC scheme leads to decreased spurious currents when compared with those obtained with the VOF-FCT scheme. This decrease is accentuated when compared with the translating case. Despite the smoothing procedure, spurious currents obtained with the VOF-PLIC-CCSF are reduced when compared with the VOF-FCT-CCSF method. This means that the shape errors introduced by the advection step are captured in the curvature calculation and overcome the errors associated with smoothed curvature calculations. Nevertheless, the spurious currents obtained with the VOF-PLIC transport schemes remain approximately 3 to 4 times greater than those

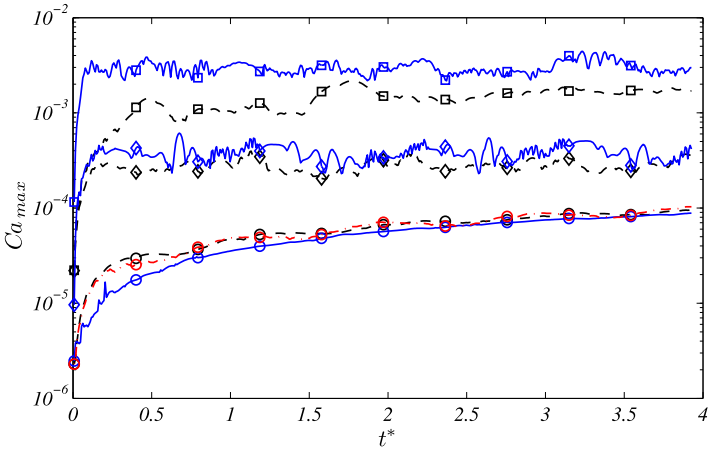

Fig. 15. Temporal evolution of the maximum velocity of spurious currents in the frame of reference moving with the bubble for $R_0/\Delta x = 12.8$, $La = 12\,000$ and $We = 30$. Legend: (—□—) VOF-FCT-CCSF; (—⊟—) VOF-FCT-HFCSF; (—◇—) VOF-PLIC-CCSF; (—◈—) VOF-PLIC-HFCSF; (—◯—) LS-CCSF; (—⊖—) LS-HFCSF; (—⊖·) LS-SSF.

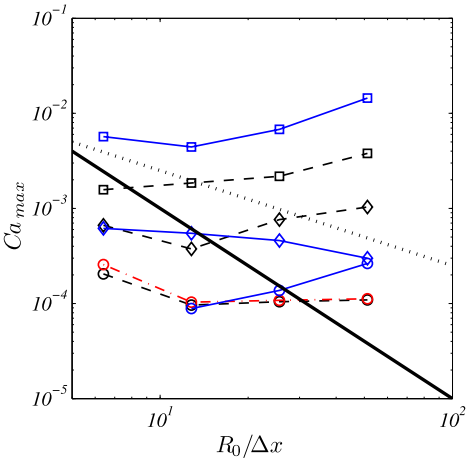

Fig. 16. Dimensionless maximum velocity of spurious currents as a function of spatial resolution for $La = 12\,000$ and $We = 30$. Legend: (—□—) VOF-FCT-CCSF; (—⊟—) VOF-FCT-HFCSF; (—◇—) VOF-PLIC-CCSF; (—◈—) VOF-PLIC-HFCSF; (—◯—) LS-CCSF; (—⊖—) LS-HFCSF; (—⊖·) LS-SSF; (· · ·) $U_{max}/U_{sigma} \sim (R_0/\Delta x)^{-1}$; (—) $U_{max}/U_{sigma} \sim (R_0/\Delta x)^{-2}$.

obtained within an LS framework where both continuous methods (LS-HFCSF and LS-CCSF) and the sharp method (LS-SSF) give identical spurious velocities.

Similarly to what happens in the translating case, the maximum and mean velocities generally do not depend on the Weber number. The trends observed for the evolution of the intensity of spurious currents with the Laplace number are also qualitatively similar to those in the translating case. However, they are more homogeneous than in the translating case, and the velocity scales approximately as $Ca_{max} \sim La^{-1/4}$ for most of the methods, except LS-CCSF and LS-SSF ($Ca_{max} \sim La^{-1/6}$).

7.1. Convergence with spatial resolution

The convergence of the different methods with spatial resolution is presented in Fig. 16, which shows the capillary number based on the maximum velocity as a function of the grid resolution. As previously observed with the translating case, with the VOF-FCT-HFCSF scheme, the intensity of spurious currents is maximum and increases with mesh resolution. Within a VOF-FCT framework, *i.e.* without interface reconstruction, the intensity of spurious currents is lower with the CCSF model than with the HFCSF scheme but the same trend with mesh refinement is observed. Similarly, the intensity of spurious currents increases as the mesh is refined with the VOF-PLIC-CCSF. At low resolution, the same intensity of spurious currents is found with the VOF-PLIC-HFCSF method but it decreases with mesh resolution. However, the rate of convergence is approximately one third, which is smaller than in the translating case (close to one). Concerning the LS transport scheme that minimizes spurious currents, while the LS-CCSF and LS-SSF methods showed a rate of convergence about 1.5 in the translating case, the magnitude of the spurious currents decreases in this flow configuration as long as the number of cells

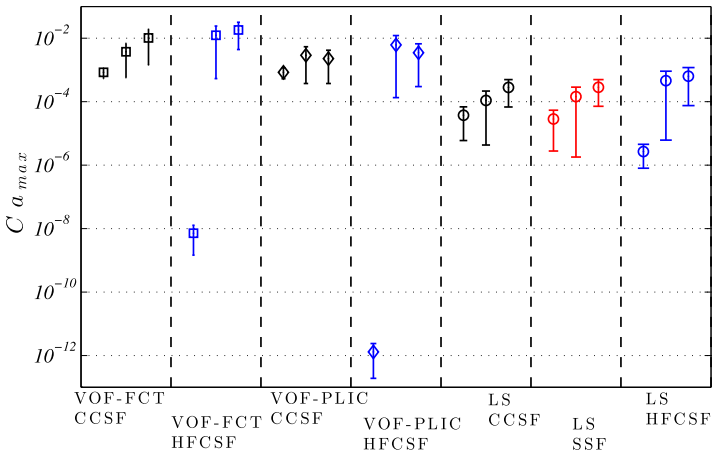

Fig. 17. Range of maximum spurious capillary number generated with the different methods for $1.2 \leq La \leq 12\,000$; $0.4 \leq We \leq 30$ and $6.4 \leq R_0/\Delta x \leq 51.2$. For each method, the static, translating and rotating cases are reported from left to right. The symbols represent the average values of spurious velocities obtained within the range of fluid properties and spatial resolution covered and the error bar corresponds to the minimum and maximum values of spurious velocities obtained.

Table 1
Summary of the main characteristics of the transport schemes and calculations of the surface tension force used for the static, translating and rotating test cases. The rates of convergence with spatial resolution, as well as the dependencies on the Laplace number, have been simplified to make the comparison easier and stress only the major differences. In order to allow an easy comparison between the methods at a common resolution of 12.8 cells per bubble radius, the spatial resolution is expressed with a modified dimensionless bubble radius $R_0^*/\Delta x = R_0/(12.8\Delta x)$. The coefficient of the scaling laws therefore corresponds to the spurious current intensity for $R_0/\Delta x = 12.8$ and $La = 1$.

Method	– spurious currents magnifier	Ca_{max} static case	Ca_{max} translating case	Ca_{max} rotating case
VOF-FCT-CCSF	– curvature calculation	10^{-3}	$1 \times 10^{-3} \left(\frac{R_0^*}{\Delta x}\right)^{0.4}$	$2 \times 10^{-2}\, La^{-\frac{1}{4}} \left(\frac{R_0^*}{\Delta x}\right)^{0.4}$
VOF-FCT-HFCSF	– advection errors	$1.4 \times 10^{-8} \left(\frac{R_0^*}{\Delta x}\right)^{-1.6}$	$2 \times 10^{-2}\, La^{-\frac{1}{4}} \left(\frac{R_0^*}{\Delta x}\right)^{0.4}$	$6 \times 10^{-2}\, La^{-\frac{1}{4}} \left(\frac{R_0^*}{\Delta x}\right)^{0.4}$
VOF-PLIC-CCSF	– curvature calculation	see VOF-FCT-CCSF	$7 \times 10^{-4} \left(\frac{R_0^*}{\Delta x}\right)^{0.2}$	$7 \times 10^{-3}\, La^{-\frac{1}{4}} \left(\frac{R_0^*}{\Delta x}\right)^{0.2}$
VOF-PLIC-HFCSF	– advection errors	10^{-12}	$5 \times 10^{-3}\, La^{-\frac{1}{4}} \left(\frac{R_0^*}{\Delta x}\right)^{-0.7}$	$5 \times 10^{-3}\, La^{-\frac{1}{4}} \left(\frac{R_0^*}{\Delta x}\right)^{-0.3}$
LS-CCSF	– curvature calculation and redistancing step	$6.1 \times 10^{-5} \left(\frac{R_0^*}{\Delta x}\right)^{-1.8}$	$4 \times 10^{-5} \left(\frac{R_0^*}{\Delta x}\right)^{-1.4}$	$5 \times 10^{-4}\, La^{-\frac{1}{6}}$
LS-HFCSF	– redistancing step and advection errors	$3.6 \times 10^{-6} \left(\frac{R_0^*}{\Delta x}\right)^{-1.3}$	$3 \times 10^{-4}\, La^{-\frac{1}{4}} \left(\frac{R_0^*}{\Delta x}\right)^{1.4}$	$10^{-3}\, La^{-\frac{1}{4}} \left(\frac{R_0^*}{\Delta x}\right)^{0.8}$
LS-SSF	– redistancing step	$5.7 \times 10^{-5} \left(\frac{R_0^*}{\Delta x}\right)^{-2.1}$	$5 \times 10^{-5} \left(\frac{R_0^*}{\Delta x}\right)^{-1.7}$	$5 \times 10^{-4}\, La^{-\frac{1}{6}}$

per bubble radius is lower than 13 but then stabilizes when refining the mesh further. The LS-HFCSF method shows the same trend as in the translating case and exhibits no convergence with spatial resolution.

Concerning the pressure errors and their convergence with grid refinement, the observations do not differ from the translating case, except that the differences between VOF-FCT and VOF-PLIC transport schemes are again enhanced. As it has been observed with the spurious velocities, the rate of convergence for the pressure jump decreases in this test case when compared with the translating one. The LS-CCSF method allows the maximum pressure jump error to be minimized but none of the methods converge with spatial resolution. The errors obtained with the VOF-FCT-HFCSF and LS-HFCSF methods increase with decreasing the cell size. It is interesting to note a difference with the translating case; although the Sharp Surface Force formulation still imposes a sharp pressure jump, this method does not appear to be superior to the VOF-PLIC-HFCSF, LS-CCSF or LS-HFCSF methods, which give the best results in this rotating flow regarding the total average pressure jump. Finally, the LS-CCSF method seems to be a good compromise between spurious current intensity and pressure jump calculation. The VOF-PLIC-HFCSF method also shows good results concerning the pressure jump estimation that are close to those obtained with the LS-CCSF method.

8. Summary of static, translating and rotating cases

A summary of the range of spurious currents observed in this study for the different methods and test cases is reported in Fig. 17 and in Table 1 through approximate correlations with the Laplace number and spatial resolution. The superiority of

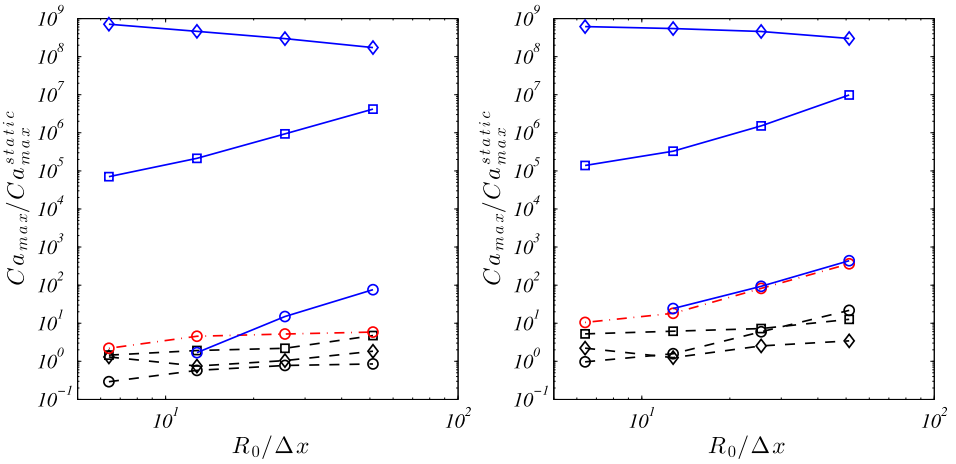

(a) Translation (b) Rotation

Fig. 18. Ratio of maximum spurious current intensity in the translating (a) and rotating (b) cases over spurious current intensity in the static case. Legend: (–□–) VOF-FCT-CCSF; (–⊟–) VOF-FCT-HFCSF; (–◇–) VOF-PLIC-CCSF; (–◈–) VOF-PLIC-HFCSF; (–◯–) LS-CCSF; (–⊖–) LS-HFCSF; (–⊙·) LS-SSF.

VOF-PLIC-HFCSF and VOF-FCT-HFCSF methods in the static case show that the accurate curvature calculation achieved with the height function method is of main importance. Figs. 18(a)–(b) show the ratio of maximum spurious current intensity in dynamic cases over that obtained in the static case. This ratio is close to one for all the CCSF methods, as well as the SSF method. This indicates that for these methods, the errors in the curvature calculation after advection in these cases are of the same order of magnitude than those obtained in a static case. With these methods, although the transport scheme can play a non-negligible role in the generation of spurious currents, these observations indicate that the main spurious currents magnifiers are the curvature calculation (and the redistancing step in LS methods) rather than the transport scheme. On the other hand, with the VOF-PLIC-HFCSF and VOF-FCT-HFCSF methods, and to a lesser extent with LS-HFCSF, the spurious currents are clearly magnified by the transport errors. Indeed, the difference between the static and dynamic cases highlights the strong interaction between interface advection and the spurious currents with an accurate curvature calculation like the height function. From a general point of view, the dynamic cases show that the curvature errors are dominated by advection errors rather than inaccurate curvature calculation and the LS methods minimize the spurious currents.

9. Taylor bubble dynamics

The present section deals with the numerical simulation of Taylor flow in microchannels, which is of practical interest since it is encountered in many applications – *e.g.* lab-on-a-chip devices, flow boiling, film coating, micro chemical reactors, etc. The motion of Taylor bubbles in microchannels is investigated with particular attention to the effects of the scalar field representing the interface and the transport scheme (VOF-FCT and LS) with a given surface tension scheme (CCSF). The LS-CCSF, which appears to be a good compromise between spurious currents generation, convergence with grid refinement and pressure calculation, is compared with the method initially implemented in *JADIM*. This flow configuration appears to be very sensitive to spurious currents since the capillary forces are often dominant (usually $Ca << 1$ and $We << 1$). In addition, the flow tends towards a stationary solution in the frame of reference moving with the bubble and spurious currents can appear when the flow is developing. The case considered here is an axisymmetrical tube with periodic boundary conditions in order to simulate a bubble train in a channel filled with a liquid. The dimensionless radius of the channel is $R^* = 1$ and the length is $L_x^* = 8$. A pressure gradient is imposed across periodic boundary conditions to induce the motion of the fluids initially at rest. The Laplace number is $La = 280$ and the capillary and Reynolds numbers vary with the imposed pressure gradient. For $Ca \geq 0.05$, the Laplace number has been reduced to $La = 2.8$ so that the Reynolds number remains lower than 10 in the present simulations. In order to correctly resolve the flow, the mesh needs to be fine enough close to the walls in order to capture the thin liquid film between the bubble and the channel wall. Furthermore, the bubble caps also need to be well resolved in order to accurately estimate the pressure jump at the rear and front caps of the bubble. The characteristics of the meshes that have been tested are summarized in Table 2 and the time step constraint due to capillary forces is indicated by making it dimensionless with the time needed for a bubble (with $Ca \sim 0.005$) to cross the domain. This dimensionless capillary time step constraint then corresponds approximately to the number of iterations that are necessary to complete one cycle in the periodic domain. The capillary time step constraint is based on the minimum cell size containing the interface instead of the minimum cell size in the whole domain.

As long as the bubble velocity is lower than the maximum velocity in the slug, as observed at low capillary numbers, the flow in the liquid slug should be composed of a recirculation loop and a film flow. When the bubble velocity is close to the mean flow velocity in the slug, the recirculation loop occupies a major part of the channel and the film is very thin [47,3].

Table 2
Different meshes used and corresponding numerical parameters.

Mesh	$N_x \times N_y$	$\Delta y_{j+1}/\Delta y_j$	Δy_{min}	$(L_x^*/U_B)/\Delta t_{cap,min}$
M1	128×32	0.9	3.967×10^{-3}	739 400
M2	128×64	0.94	1.242×10^{-3}	2 473 000

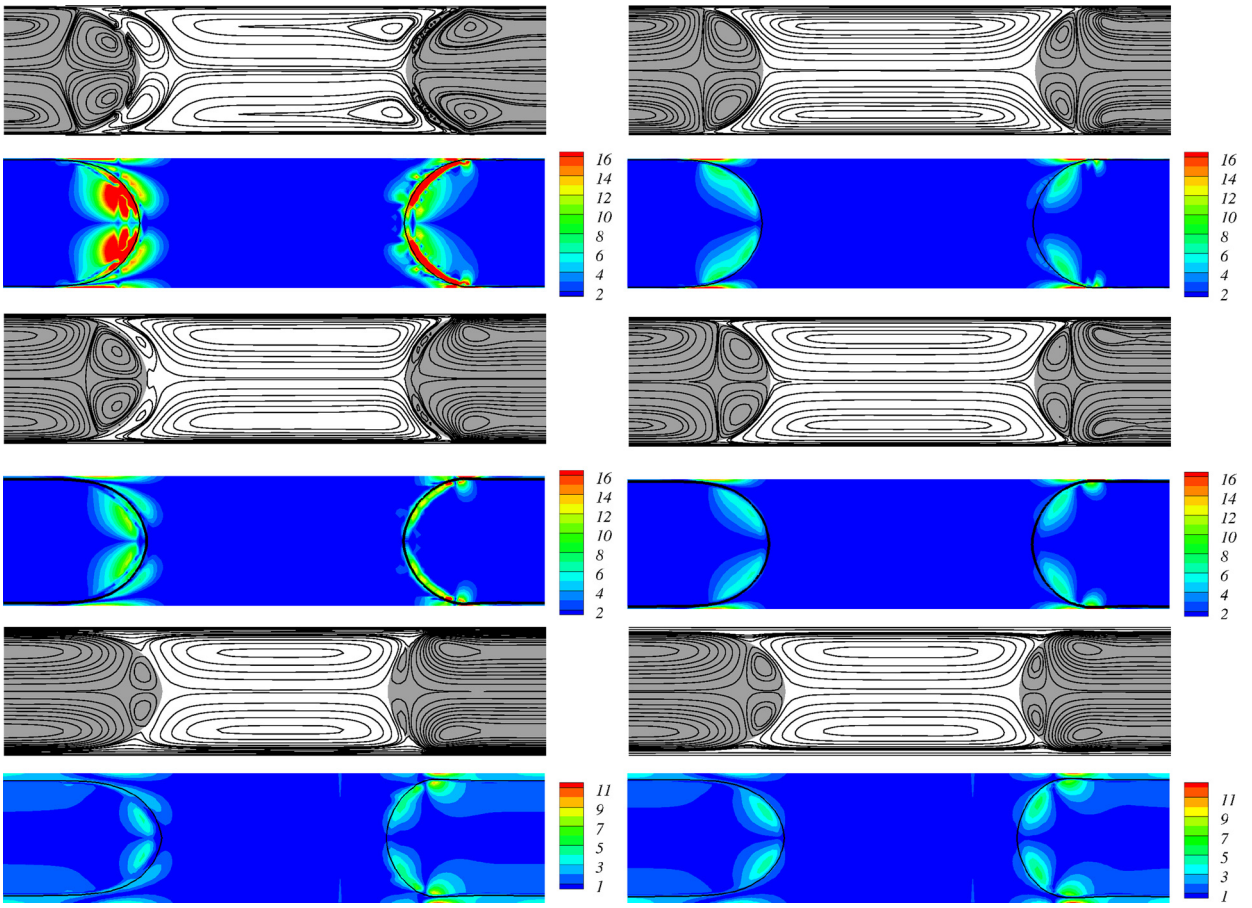

Fig. 19. Streamlines and vorticity field in Taylor flow in a microchannel. From top to bottom: $Ca = [0.002; 0.005; 0.025]$; left: VOF-FCT-CCSF, mesh 128×32; right: LS-CCSF, mesh 128×32. The vorticity field of the equivalent single phase flow of mean velocity U_{TP} has been subtracted.

Although this structure is observed qualitatively in all the LS-CCSF and the VOF-FCT-CCSF simulations for $Ca \geq 0.01$, at lower capillary numbers, the VOF-FCT-CCSF simulations present an additional liquid recirculation loop in the vicinity of the bubble nose as can be seen in Fig. 19. This phenomenon is enhanced when the number of smoothing iterations is decreased. Decreasing the capillary number, *i.e.* increasing the surface tension effects when compared to viscous forces, also enhances this phenomenon. These additional local recirculation loops are attributed to spurious currents since the vorticity generated numerically looks very similar to the spurious currents generated in the translating bubble case. The additional recirculation loop that is present in VOF-FCT-CCSF simulations decreases in size when increasing the capillary number and vanishes for a capillary number $Ca \sim 0.02$, which is in agreement with previous observations and characterization of spurious currents made with the VOF-FCT-CCSF method developed in *JADIM* [17,2]. With both an accurate curvature calculation based on height function and an accurate VOF-PLIC transport scheme, the correct flow structure was captured in [4] at low capillary numbers, down to $Ca = 0.005$, with the *Gerris* code. [24] performed similar simulations of Taylor flow with a CCSF method coupled with a VOF scheme with an artificial compression term to keep a sharp interface in a VOF without geometrical reconstruction framework. Although the authors consider that their resulting velocity field is in qualitative good agreement with the simulations of [4], the erroneous additional recirculation loop presented in Fig. 19 can also be observed in [24].

Although [20] were not able to conclude on the effects of spurious currents on the study of free bubble rise, these effects on the local velocity field in Taylor flow are clearly illustrated here. Fig. 20 shows the effects of spurious currents on the slip velocity between the bubble and the mean velocity in the slug $W = (U_B - U_{TP})/U_B$, where $U_{TP} = U_{GS} + U_{LS}$ is the sum of the gas and liquid superficial velocities. The aptitude of a method to correctly estimate this dimensionless velocity is evaluated

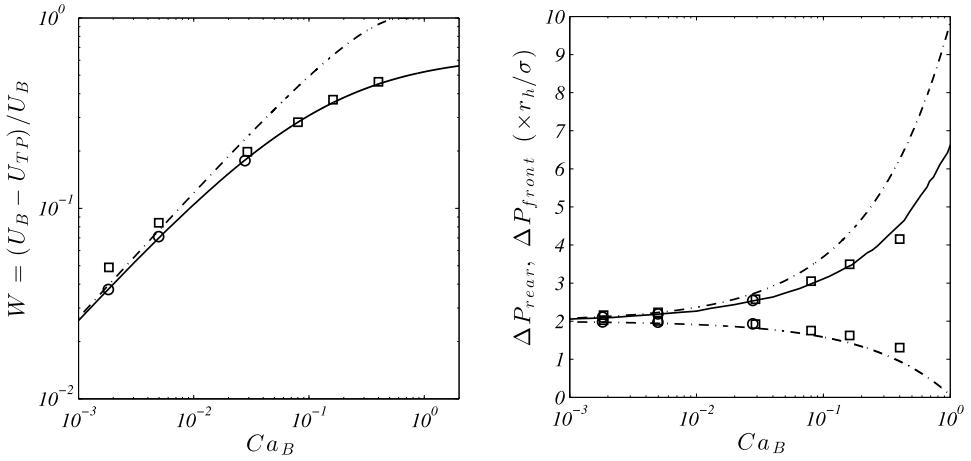

Fig. 20. (a) Dimensionless slip velocity W versus the capillary number Ca_B. Legend: (□) VOF-FCT-CCSF; (○) LS-CCSF; (dash-dotted line) Bretherton's law [9]; (straight line) Aussillous and Quéré correlation [5]. (b) Pressure drop at the front and rear caps of the bubble. Legend: (□) VOF-FCT-CCSF; (○) LS-CCSF; (dash-dotted line) Bretherton's law [9]; (straight line) results from Hazel and Heil [21].

by comparing the values obtained with the correlation proposed by Aussillous and Quéré [5] who extended Bretherton's theoretical lubrication analysis [9] to higher capillary numbers. As it was qualitatively observed with the local velocity field in Fig. 19, the difference between VOF-FCT-CCSF and LS-CCSF simulations is enhanced when the capillary number decreases. Fig. 20 shows that the LS method allows the bubble slip velocity to be accurately predicted in a wide range of capillary numbers, while the VOF-FCT-CCSF method overestimates the slip velocity and thus, the liquid film thickness since they are directly related due to the zero velocity in the liquid film surrounding the bubble. However, with both the VOF-FCT-CCSF and LS methods, the pressure drop at the front and rear caps of the bubble estimated from our simulations is in good agreement with the results from [21] who simulated the propagation of a semi-infinite bubble by solving the free surface Stokes equations with a finite-element method. The difference between both methods at the lowest capillary number simulated, which is the most sensitive to spurious currents, is only 2.4% while the difference in the slip velocity is about 30%. An advantage of the LS method is that no smoothing needs to be introduced to reduce spurious currents, whereas 12×6 smoothing iterations were employed for the computation of the curvature and orientation/spreading of the capillary force, respectively, in VOF-FCT-CCSF method as recommended in [17]. As a result, the pressure drop is sharper in the LS simulations than in the VOF-FCT-CCSF simulations.

It has generally been shown in the static, translating and rotating bubble cases that the intensity of the spurious currents obtained with the VOF-FCT-CCSF method does not decrease with spatial resolution. As a result, it is not surprising to see that the non-physical recirculation loop is not reduced with mesh size, as shown in Fig. 21 for $Ca = 0.005$. In fact, the vorticity intensity generated at the front cap of the bubble actually increases when the mesh is refined in the VOF-FCT-CCSF simulations.

The errors obtained on the dimensionless slip velocity in comparison with Aussillous and Quéré correlation are given in Table 3. It is shown that the error for a capillary number $Ca \sim 0.005$ is significant with the VOF-FCT-CCSF simulations and does not decrease significantly with mesh refinement. However, the results obtained with an LS-CCSF formulation are satisfactory even with the coarsest mesh and are in very good agreement with the correlation of Ref. [5] when the number of grid points is increased.

10. Conclusion

The generation of spurious currents and their effects on the velocity field in multiphase microfluidics has been investigated through the analysis of several numerical methods. A comparison of numerical methods comprising the transport scheme (VOF-FCT, VOF-PLIC and LS), the surface tension scheme (continuum or sharp surface force) and the curvature calculation (height function or divergence of the normal to the interface) with the same flow solver has been carried out. It can be concluded that the height function curvature calculation is very accurate and is particularly interesting for the case of static bubbles and near-static bubble or oscillating bubbles [22,19]. However, since the errors generated during the advection step are captured while they are smoothed with the convolution method, the height function method needs to be coupled with an accurate transport scheme, as it has been shown for the translating and rotating cases in this study. Otherwise, the classic CSF formulation with a smoothing of the volume fraction gives better results in terms of maximum spurious current intensity. Although the exact balance between pressure and capillary forces reached with the VOF-HFCSF methods is not achieved due to the redistancing step when using the Level Set formulation, it has been shown that the spurious

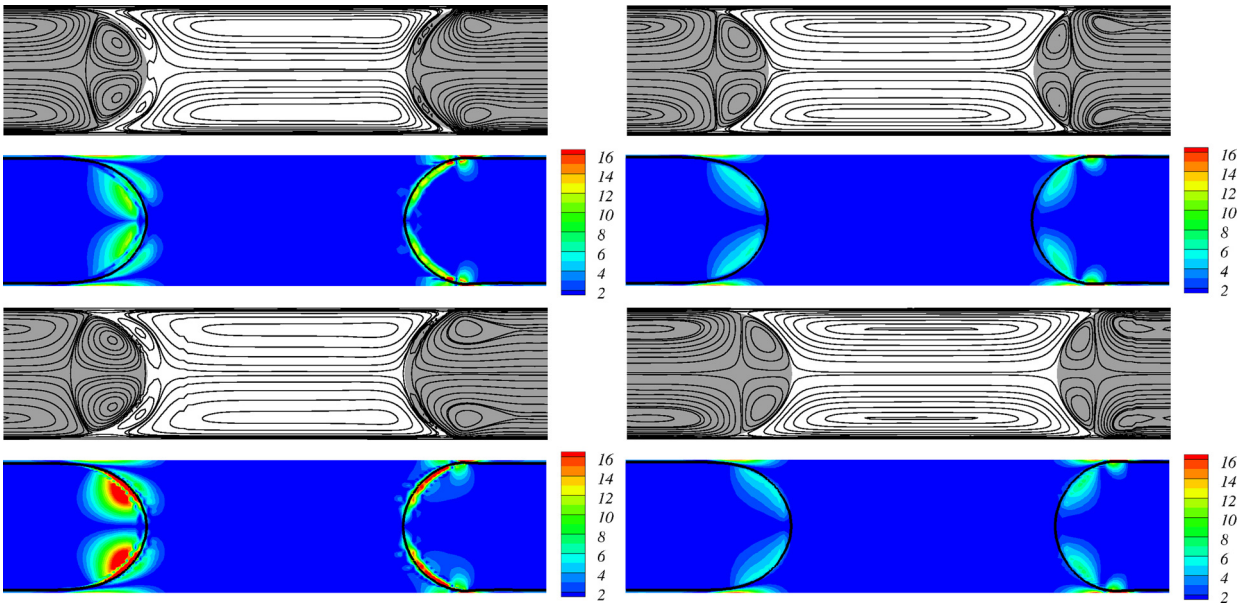

Fig. 21. Streamlines and vorticity field in Taylor flow in a microchannel ($Ca = 0.005$). Top left: VOF-FCT-CCSF, mesh 128×32; top right: LS-CCSF, mesh 128×32; bottom left: VOF-FCT-CCSF, mesh 128×64; bottom right: LS-CCSF, mesh 128×64. The vorticity field of the equivalent single phase flow of mean velocity U_{TP} has been subtracted.

Table 3
Error on the dimensionless slip velocity for a capillary number $Ca \sim 0.005$.

Mesh	$E(W)$ (VOF-FCT-CCSF)	$E(W)$ (LS-CCSF)
M1	20.44%	1.88%
M2	18.71%	0.31%

currents are decreased in dynamic cases. Similarly to the VOF-HFCSF methods, the sharp surface force that interpolates the position of the interface and the height function technique require accurate transport and redistancing schemes since they also precisely capture the slight errors created in these steps. Finally, it is shown that these test cases are well suited to the characterization of spurious currents in Taylor flow. The spurious currents generated in VOF-FCT simulations are shown to significantly modify the structure of the flow by producing an additional recirculation zone. The LS-CSF method is shown to be able to estimate the bubble slip velocity and the pressure drop across the bubble with good accuracy in a wide range of capillary numbers. In addition, since only one bubble is simulated, the global mass redistribution used in this study allows mass conservation problems to be avoided. However, cases involving several bubbles (or drops) still require additional work to resolve this mass conservation problem that occurs in classic Level Set implementations [44] since the mass redistribution algorithm used in this study ensures mass conservation in a global way but does not ensure mass conservation for each bubble (or drop). Two possible solutions may be considered in future work: the improvement of the transport scheme in a VOF framework coupled with the height function curvature calculation; and the coupling between VOF and LS methods [44]. Note that the time step convergence study has not been carried out in this paper since [18,17] showed that the time step has only minor effects on the spurious current intensity. In addition, it has been observed with the simulation of Taylor bubbles that reducing the time step leads to similar results to those obtained with the maximum time step allowed by the capillary time step constraint. Another topic that should be considered for the simulation of Taylor flows is the (semi-)implicitation of the surface tension force [25,37]. Indeed, the capillary time step as derived in [8] is very restrictive and the implicitation of the surface tension force would allow larger time steps to be used (up to twenty times the usual capillary time step constraint according to [25]), which would be of great benefit in order to reduce the computational time required for numerical simulations of surface tension driven flows.

Acknowledgements

This work was financed by the French Agence Nationale de la Recherche in the framework of the project MIGALI no. ANR-09-BLAN-0381-01. We also acknowledge the support from the FERMaT-CNRS research federation and the High Performance Computing centers CALMIP, IDRIS and CINES for providing computational resources. We would like to thank Annaïg Pedrono for the help and the support with *JADIM*. We are grateful to Stéphane Popinet for fruitful discussion about surface tension and VOF numerical schemes.

Table A.4
Effects of the different additional algorithms of the VOF-FCT advection scheme on the spurious currents for various resolutions and for $We = 30$ and $La = 12\,000$.

$R_0/\Delta x$	CCSF			HFCSF		
	12.8	25.6	51.2	12.8	25.6	51.2
VOF-FCT	$8.0082\ 10^{-4}$	$9.8943\ 10^{-4}$	$17.472\ 10^{-4}$	$2.3122\ 10^{-3}$	$2.8614\ 10^{-3}$	$5.4721\ 10^{-3}$
VOF-FCT-m	$8.0315\ 10^{-4}$	$9.9383\ 10^{-4}$	$17.472\ 10^{-4}$	$2.2229\ 10^{-3}$	$2.9478\ 10^{-3}$	$5.4721\ 10^{-3}$
VOF-FCT-mv	$9.5200\ 10^{-4}$	$11.789\ 10^{-4}$	$25.186\ 10^{-4}$	$2.9512\ 10^{-3}$	$4.8953\ 10^{-3}$	$8.6221\ 10^{-3}$
VOF-FCT-mve1	$20.187\ 10^{-4}$	$17.653\ 10^{-4}$	$26.362\ 10^{-4}$	$2.8528\ 10^{-3}$	$4.5232\ 10^{-3}$	$9.0993\ 10^{-3}$
VOF-FCT-mve2	$9.5828\ 10^{-4}$	$11.789\ 10^{-4}$	$24.518\ 10^{-4}$	$2.9582\ 10^{-3}$	$4.8954\ 10^{-3}$	$7.8929\ 10^{-3}$

Table B.5
Effects of the density ratio on the spurious currents for various resolutions and for $We = 30$ and $La = 12\,000$.

Resolution	$R_0/\Delta x = 12.8$		$R_0/\Delta x = 25.6$		$R_0/\Delta x = 51.2$	
Density ratio	$\frac{\rho_{in}}{\rho_{out}} = 1$	$\frac{\rho_{in}}{\rho_{out}} = 10^{-3}$	$\frac{\rho_{in}}{\rho_{out}} = 1$	$\frac{\rho_{in}}{\rho_{out}} = 10^{-3}$	$\frac{\rho_{in}}{\rho_{out}} = 1$	$\frac{\rho_{in}}{\rho_{out}} = 10^{-3}$
VOF-FCT-CCSF	$9.5828\ 10^{-4}$	$1.6154\ 10^{-3}$	$1.1789\ 10^{-3}$	$1.6221\ 10^{-3}$	$2.4518\ 10^{-3}$	$3.8511\ 10^{-3}$
VOF-FCT-HFCSF	$2.9528\ 10^{-3}$	$2.3206\ 10^{-3}$	$4.8954\ 10^{-3}$	$4.0643\ 10^{-3}$	$7.8929\ 10^{-3}$	$7.6236\ 10^{-3}$
VOF-PLIC-CCSF	$3.8577\ 10^{-4}$	$2.5059\ 10^{-3}$	$5.2429\ 10^{-4}$	$3.4615\ 10^{-3}$	$9.7386\ 10^{-4}$	$2.7035\ 10^{-3}$
VOF-PLIC-HFCSF	$4.6083\ 10^{-4}$	$8.2090\ 10^{-4}$	$3.0367\ 10^{-4}$	$5.3819\ 10^{-4}$	$1.7344\ 10^{-4}$	$3.0386\ 10^{-4}$
LS-CCSF	$3.5244\ 10^{-5}$	$7.5675\ 10^{-5}$	$1.3627\ 10^{-5}$	$5.8297\ 10^{-5}$	$4.2967\ 10^{-6}$	$2.9892\ 10^{-5}$
LS-HFCSF	$6.2806\ 10^{-6}$	$9.0388\ 10^{-6}$	$2.3038\ 10^{-5}$	$3.9670\ 10^{-5}$	$8.1242\ 10^{-5}$	$2.5181\ 10^{-4}$
LS-SSF	$2.5800\ 10^{-5}$	$3.8245\ 10^{-5}$	$6.9204\ 10^{-6}$	$1.6313\ 10^{-5}$	$1.8107\ 10^{-6}$	$5.3447\ 10^{-6}$

Appendix A. Choice of VOF-FCT scheme

Table A.4 shows the effects of the different features of the VOF-FCT scheme (mass redistribution, velocity extension and cut-off algorithm) on the spurious currents generated in the translating test case presented in Section 6. The Laplace number is $La = 12\,000$ and the Weber number is $We = 30$ and different spatial resolutions are used. The variants of the VOF-FCT scheme and their notations in Table A.4 are the following:

- VOF-FCT-0: original direction-split VOF-FCT scheme [51],
- VOF-FCT-1: VOF-FCT scheme [51] with mass redistribution [7],
- VOF-FCT-2: VOF-FCT scheme [51] with mass redistribution and velocity extension [7],
- VOF-FCT-3: VOF-FCT scheme [51] with mass redistribution and velocity extension, and cut-off algorithm with $nc = 1$ (see Section 2.2.2),
- VOF-FCT-4: VOF-FCT scheme [51] with mass redistribution, velocity extension, and cut-off algorithm with $nc = 2$ (see Section 2.2.2).

It is observed that the mass redistribution has no effect on the intensity of spurious currents whereas the velocity extension tends to slightly increase their intensity although it remains acceptable since the ratio is less than 1.5. Finally, it is seen that with the strict cut-off algorithm allowing only an interface thickness of one cell, the spurious current intensity can be around twice that obtained without this cut-off whereas the permissive cut-off allowing an interface thickness of two to three cells does not influence parasitic currents. Indeed, this cut-off algorithm is used only occasionally and is generally not used when the mesh is refined. Finally, it was shown in [1] with pure advection tests (circle in a shear flow for instance) that this cut-off algorithm with $nc = 2$ improves the performance of the advection step and since the effects on the spurious currents are not significant, this is the scheme that has be chosen in this study.

Appendix B. Effects of density ratio

This test case is based on the translating case introduced in Section 6 with the difference that a gas–liquid system is considered, *i.e.* the density and the viscosity in the bubble (ρ_{in} , μ_{in}) are 10^3 times lower than in the surrounding liquid (ρ_{out} , μ_{out}). The Laplace number of the continuous phase is $La = 12\,000$ and the Weber number is $We = 30$. The geometry and the meshes used are the same as in Section 6. Table B.5 shows the effects of the density ratio on spurious currents for the various methods used throughout this study and for three spatial resolutions. It is seen that the amplitude of spurious currents is nearly constant for both density ratios $\rho_{in}/\rho_{out} = 1$ and $\rho_{in}/\rho_{out} = 10^{-3}$ although the spurious current intensity is generally slightly smaller when the density ratio is unity, except for the VOF-FCT-HFCSF method. The largest difference appears with the VOF-PLIC-CCSF method where the spurious current intensity is 6.5 times higher with a density ratio of 10^{-3} than that obtained with a density ratio of 1 with the coarsest grid. The same difference is observed with the LS-CCSF method when using the finest grid. However, the differences remain less than one order of magnitude while the density ratio varies over three orders of magnitude which justifies the relevance of studying density and viscosity ratios of unity. In addition, it is noted that the rate of convergence is lower with the density ratio $\rho_{in}/\rho_{out} = 10^{-3}$ than that obtained with

$\rho_{in}/\rho_{out} = 1$. Indeed, as it is observed in Figs. 9(a) and (b), the rate of convergence of spurious currents seems to decrease slightly, especially with the LS-CCSF and LS-SSF schemes, when the Laplace number is increased. In this case, the Laplace number is one thousand times greater in the bubble ($La = 1.2 \times 10^6$) than that in the surrounding liquid ($La = 12\,000$). This is a first explanation of the lowest rate of convergence observed as the Laplace numbers differ inside and outside the bubble.

References

[1] T. Abadie, Hydrodynamics of gas–liquid Taylor flow in microchannels, PhD thesis, INP Toulouse, 2013.
[2] T. Abadie, J. Aubin, D. Legendre, C. Xuereb, Hydrodynamics of gas–liquid Taylor flow in rectangular microchannels, Microfluid. Nanofluid. 12 (2012) 355–369.
[3] T. Abadie, J. Aubin, D. Legendre, C. Xuereb, Mixing and recirculation characteristics of gas–liquid Taylor flow in microreactors, Chem. Eng. Res. Des. (2013), http://dx.doi.org/10.1016/j.cherd.2013.03.003.
[4] S. Afkhami, A.M. Leshansky, Y. Renardy, Numerical investigation of elongated drops in a microfluidic T-junction, Phys. Fluids 23 (2011) 022002.
[5] P. Aussillous, D. Quéré, Quick deposition of a fluid on the wall of a tube, Phys. Fluids 12 (2000) 2367–2371.
[6] A. Benkenida, Développement et validation d'une méthode de simulation d'écoulements diphasiques sans reconstruction d'interface. Application à la dynamique des bulles de Taylor, PhD thesis, INP Toulouse, 1999.
[7] T. Bonometti, J. Magnaudet, An interface-capturing method for incompressible two-phase flows: validation and application to bubble dynamics, Int. J. Multiph. Flow 33 (2007) 109–133.
[8] J. Brackbill, D.B. Kothe, C. Zemach, A continuum method for modeling surface tension, J. Comput. Phys. 100 (1992) 335–354.
[9] F.P. Bretherton, The motion of long bubbles in tubes, J. Fluid Mech. 10 (1961) 166–188.
[10] I. Calmet, J. Magnaudet, Large-eddy simulation of high-Schmidt-number mass transfer in a turbulent channel flow, Phys. Fluids 9 (1997) 438–455.
[11] Y.C. Chang, T.Y. Hou, B. Merriman, S. Osher, A level set formulation of Eulerian interface capturing methods for incompressible fluid flows, J. Comput. Phys. 124 (1996) 449–464.
[12] D. Chauveheid, A new algorithm for surface tension forces in the framework of the FVCF-ENIP method, Eur. J. Mech. B, Fluids 50 (2015) 175–186.
[13] F. Couderc, Développement d'un code de calcul pour la simulation d'écoulements de fluides non miscibles. Application à la désintégration assistée d'un jet liquide par un courant gazeux, PhD thesis, ENSAE, Toulouse, 2007.
[14] S.J. Cummins, M.M. Francois, D.B. Kothe, Computing curvature from volume fraction, Comput. Struct. 83 (2005) 425–434.
[15] F. Denner, B.G.M. van Wachem, Fully-coupled balanced-force VOF framework for arbitrary meshes with least-squares curvature evaluation from volume fractions, Numer. Heat Transf., Part B, Fundam. 65 (2014) 218–255.
[16] O. Desjardins, V. Moureau, H. Pitsch, An accurate conservative level set/ghost fluid method for simulating turbulent atomization, J. Comput. Phys. 227 (2008) 8395–8416.
[17] J.B. Dupont, D. Legendre, Numerical simulation of static and sliding drop with contact angle hysteresis, J. Comput. Phys. 229 (2010) 2453–2478.
[18] M.M. Francois, A balanced-force algorithm for continuous and sharp interfacial surface tension models within a volume tracking framework, J. Comput. Phys. 213 (2006) 141–173.
[19] D. Fuster, G. Agbaglah, C. Josserand, S. Popinet, S. Zaleski, Numerical simulation of droplets, bubbles and waves: state of the art, Fluid Dyn. Res. 41 (2009) 065001.
[20] D.J.E. Harvie, M.R. Davidson, M. Rudman, An analysis of parasitic current generation in Volume of Fluid simulations, Appl. Math. Model. 30 (2006) 1056–1066.
[21] A.L. Hazel, M. Heil, The steady propagation of a semi-infinite bubble into a tube of elliptical or rectangular cross-section, J. Fluid Mech. 470 (2002) 91–114.
[22] M. Herrmann, A balanced force refined level set grid method for two-phase flows on unstructured flow solver grids, J. Comput. Phys. 227 (2008) 2674–2706.
[23] C.W. Hirt, B.D. Nichols, Volume of Fluid (VOF) method for the dynamics of free boundaries, J. Comput. Phys. 39 (1981) 201–225.
[24] D.A. Hoang, V. van Steijn, L.M. Portela, M.T. Kreutzer, C.R. Kleijn, Benchmark numerical simulations of segmented two-phase flows in microchannels using the Volume of Fluid method, Comput. Fluids 86 (2013) 28–36.
[25] S. Hysing, A new implicit surface tension implementation for interfacial flows, Int. J. Numer. Methods Fluids 51 (2006) 659–672.
[26] G.S. Jiang, D. Peng, Weighted ENO schemes for Hamilton–Jacobi equations, SIAM J. Sci. Comput. 21 (2000) 2126–2143.
[27] M. Kang, R. Fedkiw, X.D. Liu, A boundary condition capturing method for multiphase incompressible flow, J. Sci. Phys. 15 (2000) 323.
[28] B. Lafaurie, C. Nardone, R. Scardovelli, S. Zaleski, G. Zanetti, Modelling merging and fragmentation in multiphase flows with SURFER, J. Comput. Phys. 113 (1994) 134–147.
[29] D. Legendre, M. Maglio, Numerical simulation of spreading drops, Colloids Surf. A 432 (2013) 29–37.
[30] D. Legendre, J. Magnaudet, The lift force on a spherical bubble in a viscous linear shear flow, J. Fluid Mech. 368 (1998) 81–126.
[31] J. López, J. Hernández, Analytical and geometrical tools for 3D volume of fluid methods in general grids, J. Comput. Phys. 227 (2008) 5939–5948.
[32] J. Magnaudet, M. Rivero, J. Fabre, Accelerated flows past a rigid sphere or a spherical bubble. Part I: Steady straining flow, J. Fluid Mech. 284 (1995) 97–135.
[33] T. Ménard, Développement d'une méthode Level Set pour le suivi d'interface – application à la rupture de jet, PhD thesis, Université de Rouen, 2007.
[34] C. Min, F. Gibou, A second order accurate level set method on non-graded adaptive cartesian grids, J. Comput. Phys. 225 (2007) 300–321.
[35] S. Popinet, Accurate adaptive solver for surface tension driven flow, J. Comput. Phys. 228 (2009) 5838–5866.
[36] S. Popinet, S. Zaleski, A front tracking algorithm for accurate representation of surface tension, Int. J. Numer. Methods Fluids 24 (1999) 775–793.
[37] M. Raessi, M. Bussman, J. Mostaghimi, A semi-implicit finite volume implementation of the CSF method for treating surface tension in interfacial flows, Int. J. Numer. Methods Fluids 59 (2009) 1093–1110.
[38] M. Raessi, J. Mostaghimi, M. Bussman, Advecting normal vectors: a new method for calculating interface normals and curvatures when modeling two-phase flows, J. Comput. Phys. 226 (2007) 774–797.
[39] Y. Renardy, M. Renardy, PROST: a parabolic reconstruction of surface tension for the volume-of-fluid method, J. Comput. Phys. 183 (2002) 400–421.
[40] M. Rudman, A volume-tracking method for incompressible multifluid flow with large density variations, Int. J. Numer. Methods Fluids 28 (1998) 357–378.
[41] F. Sarrazin, T. Bonometti, K. Loubière, L. Prat, C. Gourdon, J. Magnaudet, Experimental and numerical study of droplets hydrodynamics in microchannels, AIChE J. 52 (2006) 4061–4070.
[42] F. Sarrazin, T. Bonometti, K. Loubière, L. Prat, C. Gourdon, J. Magnaudet, Hydrodynamics structures of droplets engineered in rectangular microchannels, Microfluid. Nanofluid. 5 (2006) 131–137.
[43] M. Sussman, E. Fatemi, P. Smerecka, S. Osher, An improved level set method for incompressible two-phase flows, Comput. Fluids 27 (1997) 663–680.

[44] M. Sussman, E.G. Puckett, A coupled level set and volume-of-fluid method for computing 3D and axisymmetric incompressible two-phase flows, J. Comput. Phys. 162 (2000) 301–337.
[45] M. Sussman, P. Smerecka, S. Osher, A level set approach for computing solutions to incompressible two-phase flow, J. Comput. Phys. 114 (1994) 146–159.
[46] S. Tanguy, A. Berlemont, Application of a level set for simulation of droplet collisions, Int. J. Multiph. Flow 31 (2005) 1015–1035.
[47] G.I. Taylor, Deposition of a viscous fluid on the wall of a tube, J. Fluid Mech. 10 (1961) 161–165.
[48] D.J. Torres, J. Brackbill, The point-set method: front-tracking without connectivity, J. Comput. Phys. 165 (2000) 620–644.
[49] S.O. Unverdi, G. Tryggvason, A front-tracking method for viscous, incompressible multi-fluid flows, J. Comput. Phys. 100 (1992) 25–37.
[50] S. Zahedi, M. Kronbichler, G. Kreiss, Spurious currents in finite element based level set methods for two-phase flow, Int. J. Numer. Methods Fluids 69 (2012) 1433–1456.
[51] S.T. Zalesak, Fully multidimensional flux-corrected transport algorithms for fluids, J. Comput. Phys. 31 (1979) 335–362.